

# Thesis Title

by

E. Ross



A thesis submitted to the  
University of Birmingham  
for the degree of  
DOCTOR OF PHILOSOPHY

Solar and Stellar Physics Group (SASP)  
School of Physics and Astronomy  
University of Birmingham  
Birmingham, B15 2TT  
Month 20XX

# Contents

<b>List of Figures</b>	<b>v</b>
<b>List of Tables</b>	<b>vi</b>
<b>List of Abbreviations</b>	<b>viii</b>
<b>1 HiSPARC as a Space Weather Detector</b>	<b>1</b>
1.1 Introduction . . . . .	1
1.2 Aims . . . . .	7
1.3 HiSPARC Data . . . . .	8
1.4 Station Properties . . . . .	11
1.4.1 Cut-Off Rigidity . . . . .	11
1.4.2 Asymptotic Viewing Directions . . . . .	14
1.5 HiSPARC Observations . . . . .	15
1.5.1 Observations of Ground Level Enhancements . . . . .	15
1.5.2 Observations of Forbush Decreases . . . . .	18
1.6 Atmospheric Corrections of HiSPARC Data . . . . .	21
1.6.1 Motivation . . . . .	21
1.6.2 Barometric Correction . . . . .	23
1.6.3 Temperature Correction . . . . .	26
1.7 HiSPARC Observations After Atmospheric Corrections . . . . .	29
1.7.1 Observations of Ground Level Enhancements . . . . .	29
1.7.2 Observations of Forbush Decreases . . . . .	30
1.8 Air Shower Simulations . . . . .	33
1.8.1 Motivation . . . . .	33
1.8.2 Air Shower Footprints . . . . .	33
1.8.3 Muon Flux . . . . .	35
1.8.4 Muon Flux From MAIRE . . . . .	38
1.9 Conclusion . . . . .	43
<b>A Simulations of Cosmic Ray Air Showers using CORSIKA</b>	<b>47</b>
<b>Bibliography</b>	<b>51</b>

# List of Figures

1.1	GLEs observed by the NM stations based at Oulu. Top panel: GLE 70; middle panel: GLE 71, bottom panel: GLE 72. The solid-black line shows the 2-minute-averaged, pressure corrected data and the vertical, dashed-red lines show the epochs of each GLE onset. The units of time on the x-axis are, MM-DD HH. . . . .	6
1.2	FDs observed by the NM stations based at Oulu. Top left panel: FDs during March 2012; top right panel: FD during July 2012; bottom left panel: FD during December 2014; bottom right panel: FD during September 2017. The solid-black line shows the 2-minute-averaged, pressure corrected data and the vertical, dashed-blue lines show the epochs of each FD onset. The units of time on the x-axis are, YYYY-MM-DD. . . . .	6
1.3	The geographic location of each HiSPARC station considered in this work. Each green circle denotes the location of a detector station. . . . .	10
1.4	The availability of data for each HiSPARC station considered, for each of the space weather epochs listed in Table 1.1. The purple grids denote no available data, teal denotes that only the events data are available, and yellow denotes that both the events and singles data are available. . . . .	10
1.5	Azimuthal and zenith angle variations in the allowed and forbidden rigidity trajectories for HiSPARC station 501 from simulations in steps of rigidity, $\Delta R = 0.01$ GV. The forbidden trajectories are in black; allowed trajectories are in white. . . . .	13
1.6	The vertical asymptotic viewing directions of 5 HiSPARC stations. The rigidity range of the simulations were from $1.0 \text{ GV} < R < 20.0 \text{ GV}$ , and the results are plotted in geographic coordinates on January 20th 2005. The diamonds correspond to the HS ground location and the circles correspond to the AVD for a specific rigidity value. . . . .	15
1.7	HiSPARC data for stations 501 and 3001 around the epoch of GLE 70 on 13/12/2006. The plot shows the minute-averaged and 5-minute-averaged trigger events between detectors within the station. The vertical red, dashed line depicts the approximate onset time of the GLE. The units of time on the x-axis are, MM-DD HH. . . . .	16

1.8	HiSPARC data for stations 8001 and 3001 around the epoch of GLE 71 on 17/05/2012. The plot shows the minute-averaged and 5-minute-averaged trigger events between detectors within the station. The vertical red, dashed line depicts the approximate onset time of the GLE. The units of time on the x-axis are, MM-DD HH. . . . .	16
1.9	HiSPARC data for 4 stations around the epoch of GLE 72 on 10/09/2017. The top panel of each subplot shows the 1- and 5-minute averaged trigger events between detectors within the station, while the bottom panel shows the 1- and 5-minute averaged singles counts, mean-subtracted, for each individual detector (or signal channel, CH <sub>n</sub> ) in the station. The vertical red, dashed line depicts the approximate onset time of the GLE. The units of time on the x-axis are, MM-DD HH. . . . .	17
1.10	HiSPARC data for stations 501 and 8001 around the epoch of the FDs in March 2012. The plot shows the minute-averaged and hourly-averaged trigger events between detectors within the station. The vertical blue-dashed lines show the approximate onset-time of the FDs. The units of time on the x-axis are, YYYY-MM-DD. . . . .	19
1.11	HiSPARC data for stations 501 and 8001 around the epoch of the FD in July 2012. The plot shows the minute-averaged and hourly-averaged trigger events between detectors within the station. The vertical blue-dashed line shows the approximate onset-time of the FD. The units of time on the x-axis are, YYYY-MM-DD. . . . .	19
1.12	HiSPARC data for four stations around the epoch of the FD in December 2014. The plot shows the minute-averaged and hourly-averaged trigger events between detectors within the station. The vertical blue-dashed line shows the approximate onset-time of the FD. The units of time on the x-axis are, YYYY-MM-DD. . . . .	20
1.13	HiSPARC data for four stations around the epoch in which there were two FDs close to the onset of GLE 72. The top panel of each subplot shows the minute- and hourly-averaged trigger events between detectors within the station, while the bottom panel shows the minute- and hourly-averaged singles counts, mean-subtracted, for each individual detector (or channel, CH <sub>n</sub> ) in the station. The vertical blue-dashed lines show the approximate onset-times of the two FDs observed around this epoch and the red-dashed line depicts the approximate onset time of the GLE. The units of time on the x-axis are, YYYY-MM-DD. . . . .	22
1.14	The anti-correlation between CR count rates and the atmospheric pressure. (a) shows the CR and the local atmospheric pressure measured at a NM in the South Pole; (b) shows the CR and pressure measured by HiSPARC station 501. In both plots, the data shown is hourly-averaged, to highlight the effects. . . . .	23
1.15	The barometric coefficient calculation: (a) during November 2017 for the South Pole (SOPO) NM station, (b) during November 2019 for HiSPARC station 501 at Nikhef. . . . .	25

1.16	A comparison between the hourly-averaged HiSPARC count rate before (orange line) and after the pressure correction (blue line). . . . .	25
1.17	A comparison between the monthly barometric coefficient computed in this work and using the online barometric coefficient tool throughout the year 2017 for the SOPO NM station. . . . .	26
1.18	The relationship between the pressure corrected events data and the outdoor temperature as measured at HiSPARC station 8001 (Eindhoven). (a) shows the time-series of hourly-averaged pressure corrected events and temperature data; (b) shows the correlation between the counts and temperature, and the fitted line to calculate the correction coefficient. . . . .	28
1.19	A comparison between the hourly-averaged HiSPARC count rate before (orange line) and after the temperature correction (blue line). After the correction, the diurnal variation from the temperature effect has been reduced. . . . .	28
1.20	Atmospheric-corrected HiSPARC data for stations 8001 and 3001 around the epoch of GLE 71 on 17/05/2012. The plot shows the minute-averaged and 5-minute-averaged trigger events between detectors within the station. The vertical red, dashed line depicts the approximate onset time of the GLE. The units of time on the x-axis are, MM-DD HH. . . . .	29
1.21	Atmospheric-corrected HiSPARC data for 2 stations around the epoch of GLE 72 on 10/09/2017. The top panel of each subplot shows the 1- and 5-minute averaged trigger events between detectors within the station, while the bottom panel shows the 1- and 5-minute averaged singles counts, mean-subtracted, for each individual detector (or signal channel, CH <sub>n</sub> ) in the station. The vertical red, dashed line depicts the approximate onset time of the GLE. The units of time on the x-axis are, MM-DD HH. . . . .	30
1.22	Atmospheric-corrected HiSPARC data for station 8001 (Eindhoven) around the epoch of the FD in July 2012. The plot shows the minute- and hourly-averaged trigger events between detectors within the station. The vertical blue, dashed line depicts the approximate onset time of the FD. The units of time on the x-axis are, YYYY-MM-DD. . . . .	31
1.23	Atmospheric-corrected HiSPARC data for station 501 (Nikhef) around the epoch of the FD in December 2014. The plot shows the minute- and hourly-averaged trigger events between detectors within the station. The vertical blue, dashed line depicts the approximate onset time of the FD. The units of time on the x-axis are, YYYY-MM-DD. . . . .	31

1.24 Atmospheric-corrected HiSPARC data for 2 stations in an epoch where there were two FDs close to the onset of GLE 72. The top panel of each subplot shows the minute- and hourly-averaged trigger events. The bottom panel shows the minute- and hourly-averaged singles counts, mean-subtracted, for each individual detector (or signal channel, CH <sub>n</sub> ) in the station. The vertical blue-dashed lines show the approximate onset-times of the FDs and the red-dashed line depicts the approximate onset-time of the GLE. The units of time on the x-axis are, YYYY-MM-DD. . . . .	32
1.25 Mean muon density footprints for (a) proton-initiated air showers and (b) $\alpha$ -particle-initiated air showers with initial PCR trajectories with zenith angles $\theta = 0^\circ$ and various PCR energies. The error bars given represent $1\sigma$ . . . . .	34
1.26 Mean number of muons produced at ground level by the PCR for (a) proton-initiated air showers and (b) $\alpha$ -particle-initiated air showers, for various PCR energies. . . . .	36
1.27 Ground level muon spectra as computed in the CORSIKA simulations. (a) shows the differential muon flux at ground level; (b) shows the muon flux through a single HiSPARC detector. In both plots the solid, blue line shows the simulations using vertically incident PCRs, and the dashed, orange line shows the simulations using PCRs incident within a cone of $70^\circ$ . . . . .	37
1.28 Plots of the calculated MAIRE muon spectra for different incident PCR spectra. Blue and orange lines show muon spectra calculated for the incident GCR spectra during solar minimum and maximum, respectively. The other coloured lines show the computed muon spectra for the incident GLE spectra. (a) shows the individual muon spectra for GCRs and GLEs; (b) shows the combined muon spectra for the GCR at solar maximum and the GLEs. . . . .	39

# List of Tables

1.1	Largest space weather events since the beginning of HiSPARC, which were searched for within the HiSPARC data. The percentage-change columns provide a reference of how much the CR counts observed by the NM stations at Oulu ( $R_c=0.81$ GV) and Kiel ( $R_c=2.36$ GV) increased by or decreased by, due to the space weather event. More precise times for the event onset can be found at <a href="#">NMDB (2018)</a> (for GLEs) and <a href="#">Lingri et al. (2016)</a> (for FDs). . . . .	5
1.2	Properties of some of the HiSPARC stations: geographic longitude ( $\phi$ ), geographic latitude ( $\lambda$ ), altitude ( $h$ ), and the geomagnetic vertical cut-off rigidity ( $R_C$ ) calculated from the PLANETOCOSMICS simulations. . . . .	13
1.3	The seven GLEs where MAIRE muon spectra were available, and the maximum observed increase in the neutron flux in the NMDB and the station where the increase was observed. . . . .	38
1.4	Observed and predicted increases in the CR count rates at the Kiel NM station. The observed neutron increases use data from the NMDB, where the errors are the measurement uncertainty from the 5-minute averaged data. The predicted data for the neutrons and muons are from the MAIRE simulations. The ratio column provides a conversion factor from the MAIRE predicted neutron increases compared to those observed. The fraction column shows the proportion of the MAIRE predicted muon increase compared to the MAIRE predicted neutron increase. . . . .	40
1.5	The MAIRE predicted increase in the muon flux, adjusted for the calibration factor between observed and predicted neutron increases at the Kiel station, in Table 1.4. . . . .	41
A.1	Details of the proton-initiated air showers simulated using CORSIKA. . . . .	49
A.2	Details of the $\alpha$ -particle-initiated air showers simulated using CORSIKA. . . . .	50

# List of Abbreviations

**AMS-02** Alpha Magnetic Spectrometer.

**AS** Air Shower.

**AVD** Asymptotic Viewing Direction.

**CIR** Corotating Interaction Region.

**CME** Coronal Mass Ejection.

**CORSIKA** Cosmic Ray Simulations for Kascade.

**CR** Cosmic Ray.

**EAS** Extensive Air Shower.

**ESD** Event Summary Data.

**FD** Forbush Decrease.

**FE** Forbush Effect.

**FEID** Forbush Effects and Interplanetary-disturbances Database.

**GCR** Galactic Cosmic Ray.

**GLE** Ground Level Enhancement.

**GNMN** Global Neutron Monitor Network.

**GPS** Global Positioning System.

**HiSPARC** High School Project on Astrophysics and Research with Cosmics.

**ICME** Interplanetary Coronal Mass Ejection.

**IGRF** International Geomagnetic Reference Field.

**IMF** Interplanetary Magnetic Field.

**ISS** International Space Station.

**MAIRE** Model for Atmospheric Ionising Radiation Effects.

**MD** Muon Detector.

**NM** Neutron Monitor.

**NMDB** Neutron Monitor Data Base.

**PCR** Primary Cosmic Ray.

**PMT** Photo Multiplier Tube.

**SAPPHiRE** Simulation and Analysis Program Package for HiSPARC Research and Education.

**SCR** Solar Cosmic Ray.

**SEP** Solar Energetic Particle.

**UHECR** Ultra-High-Energy Cosmic Ray.

# 1 HiSPARC as a Space Weather Detector

## 1.1 Introduction

The observation of Cosmic Rays (CRs) provides a tool to monitor the effects of space weather on Earth. Space weather events have been regularly monitored by ground-based CR detectors since the early 20th Century (Forbush, 1937; Kudela et al., 2000; Schwenn, 2006) and the detectors have been instrumental in characterising the environments surrounding space weather events.

Short-term increases in the Galactic Cosmic Ray (GCR) flux were first observed in the 1940s and early 1950s, but it wasn't until after the largest recorded event in September 1956 that these increases were defined as Ground Level Enhancements (GLEs) (Cramp, 1996). GLEs are the detection of an increased number of the highest-energy portion ( $> 500$  MeV, Kuwabara et al. 2006b) of Solar Energetic Particles (SEPs) arriving at Earth following a solar eruptive event (McCracken et al., 2012; Poluianov & Usoskin, 2017). The SEPs, which cause GLEs, can cause serious damage to satellite electronics and are a hazard to air crew and astronauts; hence, the monitoring of these events are of importance for space weather forecasting.

The total number of GLEs observed to-date is low, there have been only 72. The GLE database<sup>1</sup> is a record of events measured using the Global Neutron Monitor Network (GNMN), starting from GLE 5 (February 1956), since the beginning of CR space weather monitoring operations (Usoskin et al., 2016). Many studies have investigated the observations of GLEs, analysing their characteristics, as well as the

---

<sup>1</sup><https://gle.oulu.fi>

spectra and anisotropy of Primary Cosmic Rays (PCRs) that produce the GLEs; for an overview see: [Shea & Smart \(1982\)](#); [Cramp \(1996\)](#); [Belov et al. \(2010\)](#); [McCracken et al. \(2012\)](#); [Strauss et al. \(2017\)](#); [Mishev et al. \(2018\)](#).

In addition, a GLE real-time alarm system was developed by [Kuwabara et al. \(2006a,b\)](#), using data from Neutron Monitors (NMs) and Muon Detectors (MDs), which has been shown to provide the earliest alert for the onset of SEP-driven space weather events. They showed their alerts provide a warning up to an hour earlier than the storm onset. Furthermore, they also show that through utilising the GNMN, monitoring precursory anisotropy, they can also issue warnings several hours ahead of near-Earth, in-situ satellite observations. They state that using both NMs and MDs provides a dual energy range for observations, providing a more effective system.

On this dual energy range for space weather observations; NMs generally observe PCRs with energies  $\sim 1 - 10$  GeV and above, while MDs typically observe higher energy PCRs with energies on the order of  $\gtrsim 10$  GeV ([Kuwabara et al., 2006a](#); [Rockenbach et al., 2014](#)). After a solar eruptive event, it is expected that the first particles to arrive at Earth are those with higher energies and that traverse the shortest distance, i.e. travelling along the Interplanetary Magnetic Field (IMF) ([Kuwabara et al., 2006a](#)). Different behaviours observed between MDs and NMs are linked with the different particle species observed by these two detectors and the signal at MDs can therefore be linked with the maximum flare energy release and an earlier arrival of the SEPs at Earth ([Kuwabara et al., 2006a](#)).

Short-term decreases in the GCR flux were first observed by [Forbush \(1937\)](#) and therefore were later coined as Forbush Decreases (FDs) or Forbush Effects (FEs). There are two types of FD: one caused by Corotating Interaction Regions (CIRs) ([Dumbović et al., 2016](#)), and one caused by Interplanetary Coronal Mass Ejections (ICMEs) and the shocks they drive ([Belov, 2008](#)). The biggest FDs (magnitudes  $> 5\%$ ) are strictly associated with ICMEs ([Belov et al., 2001](#)). Of the kind caused

by ICMEs, the majority of are produced by ICMEs with speeds in the range 400 – 1200 km s<sup>-1</sup> (Lingri et al., 2016); the typical speed of the solar wind is, for slow solar wind, in the range: 300 – 400 km s<sup>-1</sup>, and for fast solar wind,  $\sim$  750 km s<sup>-1</sup> (Owens & Forsyth, 2013). In addition, Belov et al. (2001, 2014) showed the magnitude of the FD is proportional to the speed, mass, and width of the Coronal Mass Ejection (CME). We also see from the Neutron Monitor Data Base (NMDB) data, generally, the magnitude of the FD is also inversely proportional to the PCR energy.

The Forbush Effects and Interplanetary-disturbances Database (FEID)<sup>2</sup> is a record of all the FDs observed since the beginning of the GNMN (Belov, 2008). The total number of events is  $\sim$  7630 during the epoch 1957 –2020. Many studies have discussed the observations of FDs and investigate their features, driving factors, and precursors; for an overview see: Belov et al. (2001); Usoskin et al. (2008); Wawrzynczak & Alania (2010); Rockenbach et al. (2014); Arunbabu et al. (2015).

The variation in CR counts during space weather events, as measured by several stations with different rigidities across the GNMN, shows a larger GLE or FD magnitude is generally observed for lower rigidity PCRs. Belov et al. (2005) claimed a relationship between the variation and the rigidity was approximately  $\propto R^{-0.8}$ , showing a clear inverse relationship between rigidity and degree of count variation.

Despite most observations of space weather events in the literature utilising data acquired by NMs, there are some reports of observations with MDs also. However, in general, the MD observations of space weather events are significantly less pronounced than the measurements using NMs for both GLEs (Timashkov et al., 2008; Augusto et al., 2016) and FDs (Braun et al., 2009; Rockenbach et al., 2014), due to the higher rigidity PCRs they observe. This suggests that MDs may not be the most suitable instrument for monitoring space weather events, and highlights why NMs are routinely used.

The High School Project on Astrophysics and Research with Cosmics (HiSPARC)

---

<sup>2</sup><http://spaceweather.izmiran.ru/eng/dbs.html>

was set up with the detection philosophy of observing Extensive Air Showers (EASs) of muons, which are typically associated with PCRs with energy of  $\sim 10^{14}$  eV and above, that produce large footprints observable with many HiSPARC stations simultaneously (Fokkema, 2012; Bartels, 2012). For PCRs with energies below  $\sim 10^{14}$  eV the induced air shower is small, with almost no observable muon footprint, and for PCRs with energy below  $\sim 10^{11}$  eV, there are typically fewer than one or two muons that reach the ground, making their observation difficult (van Dam et al., 2020). Most muons produced by such low-energy PCRs decay higher in the atmosphere and their energy is mostly transferred into the resultant electron (van Dam et al., 2020), but depending on the electron energies, they are also observable by HiSPARC.

The HiSPARC detectors have, individually, a high muon-detection efficiency close to 100% (van Dam et al., 2020), therefore they are capable of observing any muons that traverse them. This project was hence motivated by the existing network of MDs which may have the capability of observing the CRs associated with space weather events.

In the literature there exists no previous work which investigates the use of the HiSPARC network to monitor space weather. Previous studies using HiSPARC data have only considered PCRs with energies  $> 10^{12}$  eV, therefore several orders of magnitude larger than the energies usually associated with space weather events. This is due to the heritage of the HiSPARC network in observing Ultra-High-Energy Cosmic Rays (UHECRs). In this work, we provide a feasibility study to investigate whether the existing HiSPARC network is capable of observing space weather events.

Few space weather events have been observed over the lifetime of the HiSPARC network; however, Table 1.1 outlines the specific GLEs and FDs that occurred since the beginning of HiSPARC that were investigated in this work. The table also shows, for reference, the magnitude of the CR count variation observed by two NMs: Oulu, Finland ( $R_c=0.81$  GV), and Kiel, Germany ( $R_c=2.36$  GV), where  $R_c$  is the rigidity

cut-off and is the minimum rigidity PCR observable by the stations due to the Earth's geomagnetic field.

Table 1.1: Largest space weather events since the beginning of HiSPARC, which were searched for within the HiSPARC data. The percentage-change columns provide a reference of how much the CR counts observed by the NM stations at Oulu ( $R_c=0.81$  GV) and Kiel ( $R_c=2.36$  GV) increased by or decreased by, due to the space weather event. More precise times for the event onset can be found at [NMDB \(2018\)](#) (for GLEs) and [Lingri et al. \(2016\)](#) (for FDs).

GLE Onset	GLE	% Change		FD Onset	% Change	
		Oulu	Kiel		Oulu	Kiel
13/12/2006	70	~ 90%	~ 30%	08/03/2012	~ 10%	~ 10%
17/05/2012	71	~ 15%	~ 3%	12/03/2012	~ 3 – 5%	~ 3 – 5%
10/09/2017	72	~ 5%	N/A	14/07/2012	~ 3 – 5%	~ 5 – 10%
				21/12/2014	~ 5 – 10%	~ 5 – 10%
				06/09/2017	~ 1 – 2%	N/A
				07/09/2017	~ 6%	N/A

The specific events in Table 1.1 were selected as: (i) for the GLEs, they are the only three that occurred in the HiSPARC operational period; (ii) for the FDs, they are among the most recent FDs that result in a NM count-rate variation in excess of  $\sim 5\%$  and the largest FDs are likely to be the most promising candidates for observation with HiSPARC.

For reference, and later comparison with the HiSPARC results, we show the GLEs, as observed by the Oulu NM station, in Finland, using data taken from the NMDB, in Figure 1.1. In Figure 1.1 we see that the relative increase of the CR counts during the GLE was large for GLEs 70 and 71, but much lower during GLE 72. For each GLE, the increase is easily observable by-eye in the data. We expect that if we are to observe any of the GLEs, we shall have the best chance of observing GLE 70. Similarly, we show a plot of the FDs, as observed by the Oulu NM station, in Figure 1.2.

Each FD in Figure 1.2 produces a moderate decrease in the NM count rate. The relative decreases in the the CR counts during the FDs were generally around  $\sim 5\%$ , and are easily observable by-eye in the data.

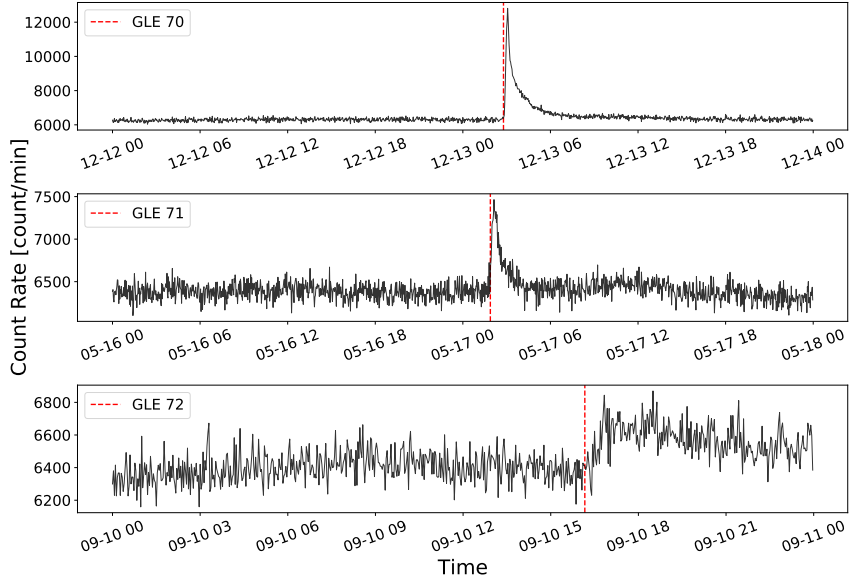


Figure 1.1: GLEs observed by the NM stations based at Oulu. Top panel: GLE 70; middle panel: GLE 71, bottom panel: GLE 72. The solid-black line shows the 2-minute-averaged, pressure corrected data and the vertical, dashed-red lines show the epochs of each GLE onset. The units of time on the x-axis are, MM-DD HH.

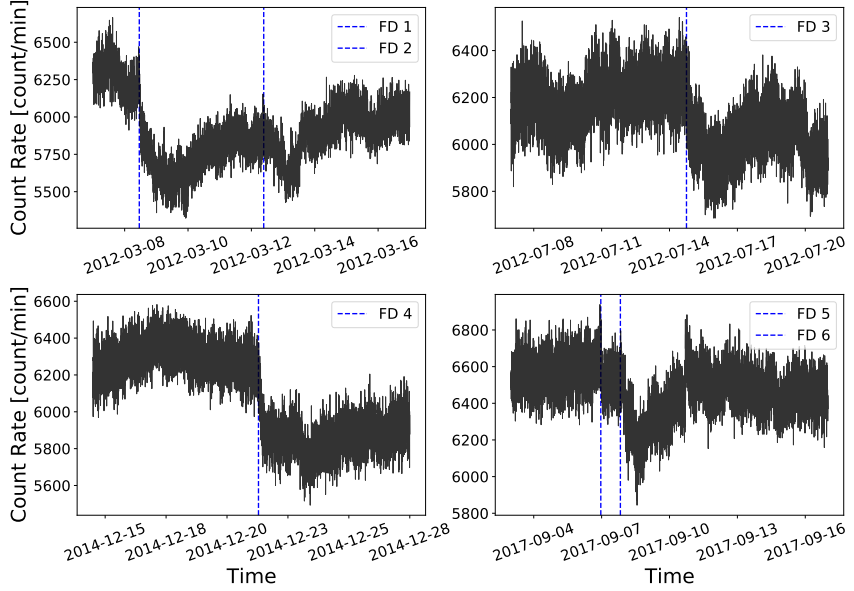


Figure 1.2: FDs observed by the NM stations based at Oulu. Top left panel: FDs during March 2012; top right panel: FD during July 2012; bottom left panel: FD during December 2014; bottom right panel: FD during September 2017. The solid-black line shows the 2-minute-averaged, pressure corrected data and the vertical, dashed-blue lines show the epochs of each FD onset. The units of time on the x-axis are, YYYY-MM-DD.

## 1.2 Aims

The principle aim of the project was to determine whether the existing HiSPARC network is capable of observing space weather events. To do this, we initially calculated the properties of the HiSPARC detectors, to understand the typical PCRs they observe. In addition, we investigated the data during periods of space weather activity to search for the associated signatures detailed in Table 1.1. We searched through some of the most reliable HiSPARC stations to determine whether these events were observed in the data. This was done to determine whether, without much effort, we could get a binary answer on whether these events were observed by HiSPARC.

Ground-based observations of muons from air showers are susceptible to the conditions in the atmosphere; where possible, we aimed to correct for these atmospheric effects and again reviewed the corrected data to determine whether the space weather events were observed.

Finally, we also aimed to perform simulations of air showers initiated by CRs to understand the expected muon flux and dispersion at ground level. This would help us to understand how likely it is to observe the PCRs associated with space weather with the HiSPARC detectors, observing muons.

It was highlighted during private communication with the UK Met Office that observations of GLEs are of more interest and importance to space weather forecasts and nowcasts. As discussed above, using MDs generally provides observations of higher energy PCRs which relates to the earlier onset of SEPs; thus using the HiSPARC network is of significant interest in this domain. FDs are of lower interest and importance; however, we still searched for FDs within the HiSPARC data for completeness.

## 1.3 HiSPARC Data

The HiSPARC cosmic ray data are available on the HiSPARC Public Database<sup>3</sup>, where each station is listed, grouped by local nodes. For every station one can see its ID, name, and a coloured square and circle displaying its current data delivery and data acquisition status, respectively. Clicking on any station takes you to a dedicated page which displays its data on a user-selected day. Where data are available, it is possible to download:

- events rate data: where multiple detectors in a station are triggered to satisfy that station’s trigger condition;
- singles rate data: the count rates of the individual detectors within a station;
- weather data: meteorological data, including pressure and temperature;
- coincidences data: the counts where different stations measure the same event (to within 1.36  $\mu$ s); it is possible to determine if stations measured the same event by comparing the Global Positioning System (GPS) timestamps of events.

This method of obtaining HiSPARC data is acceptable if only a small quantity of data are needed, but it is cumbersome if large quantities of data are required. To obtain large quantities of HiSPARC data, it was more efficient to use the Event Summary Data (ESD) module within the Simulation and Analysis Program Package for HiSPARC Research and Education (SAPPHiRE) Python package ([Fokkema et al., 2012](#)). The data are downloaded in the raw HDF5 format, and can then be manipulated using further Python scripts.

A Python script was written, which used the SAPPHiRE ESD module, to request the download of a specific type of data (i.e. events, singles, weather), from a user-specified station, download and open the HDF5 table, manipulate the data to either keep them in the raw cadence or resample into other timebases, and finally store the

---

<sup>3</sup><https://data.hisparc.nl/>

data in .csv format. This reduced the complexity involved in downloading the data and provided a repeatable method of acquiring the HiSPARC data in a consistent format.

There exists some  $\sim 140$  stations in the HiSPARC network ([van Dam et al., 2020](#)) which have been uploading data for varying durations since 2005. It was too challenging to acquire and analyse data from every station, hence a smaller sample of 5 stations was selected for investigation. The stations in the sample are outlined in Table 1.2, a mixture of 2-detector and 4-detector stations. Approximately 110 of the  $\sim 140$  stations record singles rates, which have only been available since 2016, and only 29 stations acquire weather data. In general, throughout the history of the HiSPARC network, the availability of weather data is irregular and many stations that acquire the data go through periods of acquiring no meteorological data at all, which made the selection of stations non-trivial.

The 5 stations in the sample were selected as they generally have both the singles and weather data available, with the exception of station 14001 (Birmingham University). Station 14001 only came online in 2014; it does not acquire weather data and did not begin acquiring singles data until February 2019, but it was deemed necessary to include this station as it is maintained by the University of Birmingham, therefore we have full control over the operation of the station and is a useful reference. Station 501 (Nikhef) is the original station in the network, and serves as the ‘gold standard’ for HiSPARC, therefore it was included. The other three stations all showed good data quality in terms of data availability and consistent operating conditions. The stations are shown on a map in Fig. 1.3.

Figure 1.4 shows the availability of CR data for the sample of stations for each of the space weather events investigated, where purple grids denote no available data, teal denotes events data were available, and yellow denotes events and singles data were available. For each event, we have data available from at least two stations, which allows us to compare the signals. It also shows as the HiSPARC network



Figure 1.3: The geographic location of each HiSPARC station considered in this work. Each green circle denotes the location of a detector station.

matures, so does the number of stations with available data, and the type of data available (both events and singles rates).

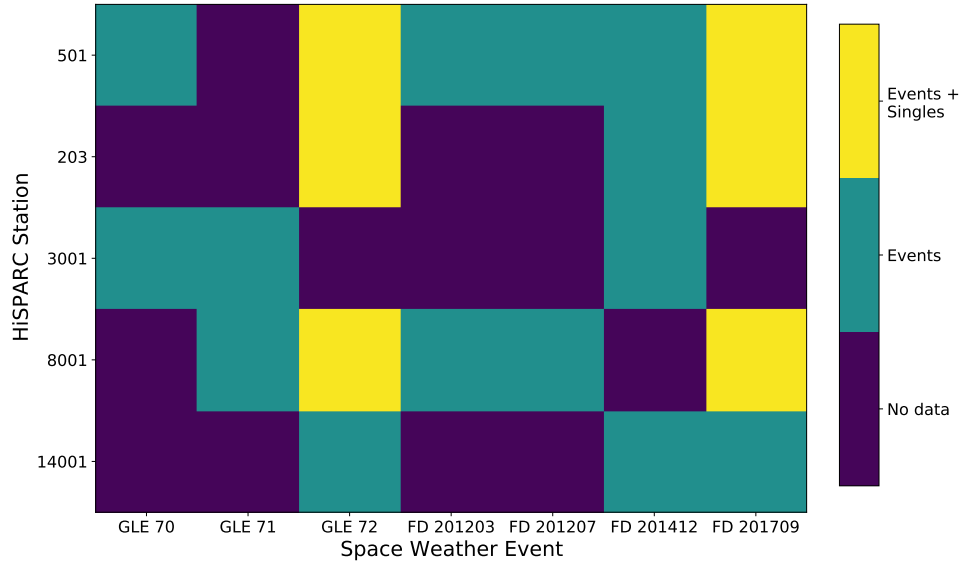


Figure 1.4: The availability of data for each HiSPARC station considered, for each of the space weather epochs listed in Table 1.1. The purple grids denote no available data, teal denotes that only the events data are available, and yellow denotes that both the events and singles data are available.

## 1.4 Station Properties

### 1.4.1 Cut-Off Rigidity

To understand the PCR spectrum that ground-based CR detectors may observe, PCR transport simulations are typically performed. The geomagnetic field can prohibit CR particles from penetrating the magnetosphere and reaching the atmosphere, depending on the particle’s energy. As a consequence, the cut-off rigidity is an estimate of the lower rigidity-threshold, below which the particle flux is zero due to geomagnetic shielding (measured in Volts, V, or Gigavolts, GV) ([Shea et al., 1965](#); [Danilova et al., 2019](#)). Transport simulations allow us to determine the range of PCRs that have sufficient energy to penetrate the Earth’s magnetosphere and reach the atmosphere and produce secondary particle air showers. The PCR spectrum depends strongly on the geographic location of the station; the minimum allowed particle rigidity varies from  $\sim 17$  GV near the equator and theoretically 0 GV at the poles, and the geomagnetic conditions have a strong impact on the PCR spectrum ([Shea et al., 1965](#); [Cramp, 1996](#); [Desorgher et al., 2006](#); [Danilova et al., 2019](#)).

Transport simulations typically run a reverse evolution of particles, using a backwards-tracing routine, whereby the particles are simulated from Earth out to the magnetosphere, to determine whether they leave the magnetosphere or remain trapped due to the geomagnetic field ([Shea et al., 1965](#)). In this work, to perform the PCR transport simulations we used the PLANETOCOSMICS software ([Desorgher, 2005](#)). PLANETOCOSMICS performs Geant4 Monte Carlo simulations of charged particle transport through Earth’s magnetosphere based on Størmers transport equation for charged particles ([Desorgher, 2005](#); [Desorgher et al., 2006](#)).

PLANETOCOSMICS simulates backward trajectories of charged particles from a given location (latitude, longitude, and altitude) out to the magnetopause for a set of PCR rigidities. For each simulated trajectory there are two possible outcomes: (i) the particles trace out to the magnetopause where they escape Earth’s

magnetosphere, an allowed trajectory; (ii) the particles are sufficiently bent by the effect of the Earth’s magnetosphere that they do not reach the magnetopause and cannot escape the Earth’s magnetosphere, a forbidden trajectory (Shea et al., 1965; Desorgher, 2005; Desorgher et al., 2006). The coordinates of the asymptotic direction at the magnetosphere are provided as an output from the simulations. This is the direction of motion of particles upon leaving the magnetosphere, if subjected to no other forces (Shea et al., 1965; Desorgher et al., 2006; Danilova et al., 2019). In this work PLANETOCOSMICS was configured with the Tsyganenko-89 model for the external magnetospheric magnetic field (Tsyganenko, 1989, 2013) and the International Geomagnetic Reference Field (IGRF) internal field model (Thébault et al., 2015).

Each simulated rigidity, whether it followed an allowed or forbidden trajectory, was stored and was used to provide an insight into the rigidity spectrum for a given station. From the allowed trajectories the effective cut-off rigidity ( $R_C$ ) for the stations was computed, which represents the lower rigidity limit above which cosmic rays can cross the magnetosphere and reach the atmosphere:

$$R_C = R_U - \sum_{i=R_L}^{R_U} \Delta R_i \quad (1.1)$$

where  $R_U$  is the upper rigidity (the last allowed trajectory before the first forbidden trajectory);  $R_L$  is the lower rigidity (the last allowed trajectory before which all other trajectories with a lower rigidity are forbidden);  $\Delta R$  is the rigidity step size in the simulation (Shea et al., 1965; Desorgher, 2005; Desorgher et al., 2006; Herbst et al., 2013).

The rigidity spectrum for each of the five HiSPARC stations was investigated to determine  $R_C$  for each station. The cut-off rigidity calculated for the five HiSPARC stations for a vertical incidence upon the atmosphere (i.e.  $0^\circ$  zenith angle) are shown in Table 1.2 which show that there is little variation in  $R_C$  between the HiSPARC stations and that they observe protons with rigidities in excess of  $\sim 3$  GV.

Table 1.2: Properties of some of the HiSPARC stations: geographic longitude ( $\phi$ ), geographic latitude ( $\lambda$ ), altitude ( $h$ ), and the geomagnetic vertical cut-off rigidity ( $R_C$ ) calculated from the PLANETOCOSMICS simulations.

Station Name/ID	$R_C$ [GV]	$\phi$ [deg]	$\lambda$ [deg]	$h$ [m]	No. Detectors
Nikhef/501	3.19	4.95 E	52.36 N	56.18	4
College Hageveld/203	3.18	4.63 E	52.35 N	53.71	2
Leiden/3001	3.23	4.45 E	52.17 N	54.08	2
Eindhoven/8001	3.44	5.49 E	51.45 N	70.12	2
Birmingham University/14001	3.06	1.93 W	52.45 N	204.14	4

This analysis was initially carried out for the vertical direction (i.e. azimuth =  $0^\circ$ , zenith =  $0^\circ$ ); however further trajectories were simulated for different azimuth and zenith angles to determine the dependence of the rigidity spectrum on the detector acceptance angle. The analysis for the azimuthal dependence was carried out at a zenith angle of  $20^\circ$  as this is around the most probable angle for HiSPARC events (Fokkema, 2012), and the analysis of the zenith dependence was carried out at an azimuth angle of  $0^\circ$ . This analysis is shown in Figure 1.5, and demonstrates that there is no strong dependence of the azimuth direction or zenith (up to  $45^\circ$ ).

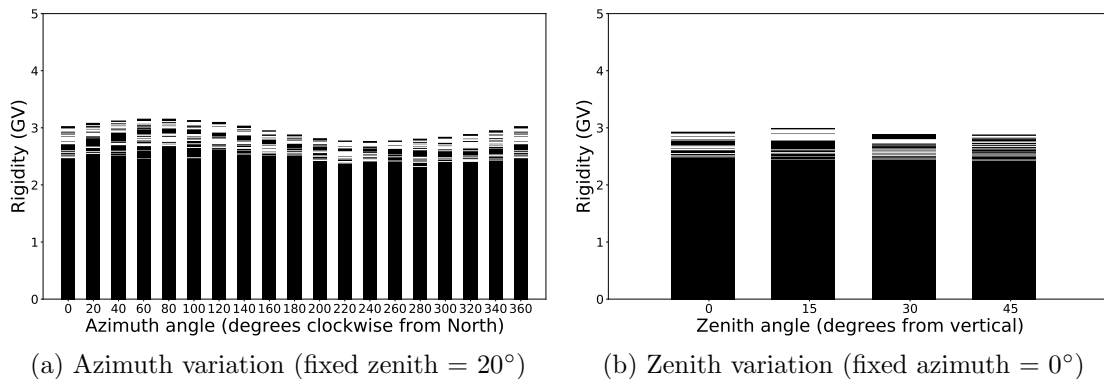


Figure 1.5: Azimuthal and zenith angle variations in the allowed and forbidden rigidity trajectories for HiSPARC station 501 from simulations in steps of rigidity,  $\Delta R = 0.01$  GV. The forbidden trajectories are in black; allowed trajectories are in white.

The small variation between HiSPARC stations is due to their close proximity in geographic latitude and longitude. The values of  $R_C$  calculated for the HiSPARC stations suggest that they should be able to observe higher energy Solar Cosmic Ray

(SCR), but may not be as susceptible as the higher latitude NMs where the effects of GLEs are highly observable.

### 1.4.2 Asymptotic Viewing Directions

Another output from the PLANETOCOSMICS simulations allowed us to understand the directions of moving particles entering the Earth’s magnetosphere prior to their trajectory through the magnetosphere and arrival at the atmosphere. By tracking particle trajectories we can define the Asymptotic Viewing Direction (AVD) of CR stations, which represents the direction of CR motion before entering the magnetosphere and being observed by a detector ([Danilova et al., 2019](#)). This allowed us to understand the directions in space that ground-based CR detectors observe. Higher energy CRs are deflected less by the magnetosphere and therefore the AVDs of high rigidity cut-off stations are simply their zenith; however, lower energy CRs are deflected more, there stations with a lower rigidity cut-off may observe CRs from a range of directions.

It can be seen from Figure 1.6 that the AVDs for each of the HiSPARC stations investigated are rather similar, due to their close geographic proximity, and that they mostly straddle the equator for low rigidity PCRs.

The simulations were performed up to a rigidity of 20 GV, in steps of  $\Delta R = 0.01$  GV, and the AVDs are limited between  $\pm 20^\circ$  latitude. However, at higher rigidities, we would see the AVDs spiral in towards the geographic location of the station, and the PCR would enter the magnetosphere and atmosphere almost vertically above the detector. The 20 GV directions are all grouped closely together due to the close geographic locations of the stations. This map of the AVDs also informs us that we should expect to be able to observe some lower energy PCRs when the zenith of the detector is not facing the asymptotic direction of the PCR. The viewing directions of allowed, lower rigidity, trajectories with  $R_C \sim 2.5$  GV are shifted East by  $\sim 120^\circ$  longitude. This demonstrates that the observable, lower-energy PCRs are

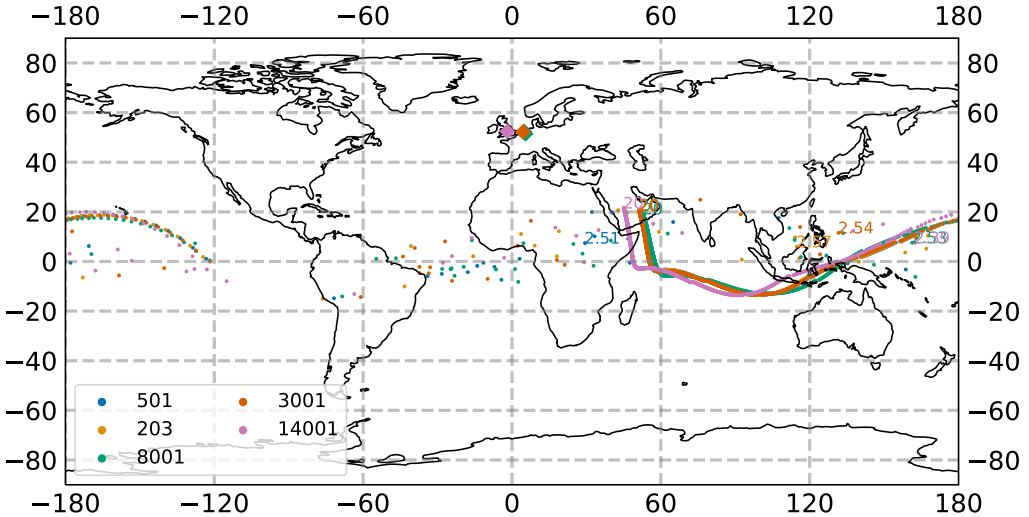


Figure 1.6: The vertical asymptotic viewing directions of 5 HiSPARC stations. The rigidity range of the simulations were from  $1.0 \text{ GV} < R < 20.0 \text{ GV}$ , and the results are plotted in geographic coordinates on January 20th 2005. The diamonds correspond to the HS ground location and the circles correspond to the AVD for a specific rigidity value.

deflected significantly by the Earth's magnetosphere; we can observe solar eruptive events when the station is not pointing in a direction in-line with the Sun therefore may observe particles from this direction some  $\sim 8$  hours before the stations align with the direction of the source.

This has significant impacts on the ability of our detectors to observe transient solar eruptive events which may be highly anisotropic and have a SEP spectrum with energies  $< 10^9 \text{ eV}$ . For this reason, many ground-based CR stations are spread across Earth's surface, to maximise the observation coverage.

## 1.5 HiSPARC Observations

### 1.5.1 Observations of Ground Level Enhancements

The search for evidence of GLEs within the HiSPARC data was conducted for the events listed in Table 1.1, as they are the only GLEs that span the operational epoch of the HiSPARC network. Figure 1.7, 1.8, and 1.9 show the HiSPARC observations around GLE 70, 71, and 72, respectively. As highlighted by Fig. 1.4, most of the observations are only the events data (i.e. coincidences between the detectors of a

station); however, where possible, we also show the singles rates from each of the individual detectors in a station, when available.

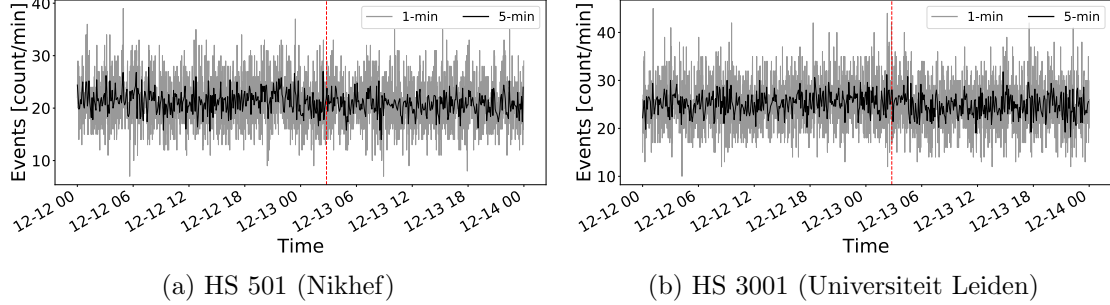


Figure 1.7: HiSPARC data for stations 501 and 3001 around the epoch of GLE 70 on 13/12/2006. The plot shows the minute-averaged and 5-minute-averaged trigger events between detectors within the station. The vertical red, dashed line depicts the approximate onset time of the GLE. The units of time on the x-axis are, MM-DD HH.

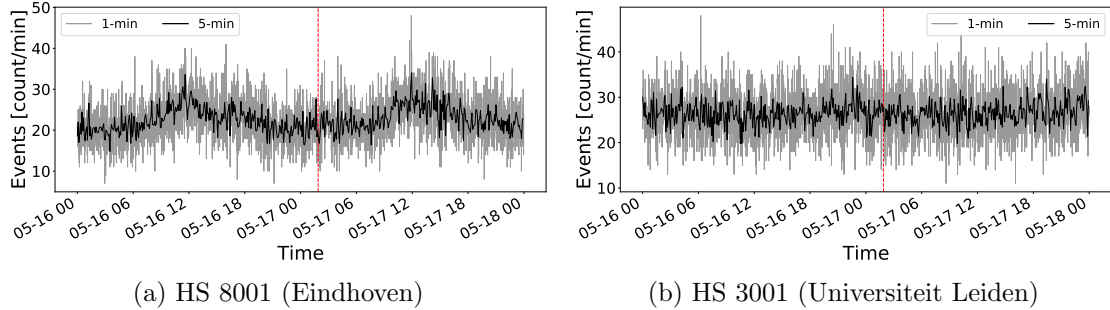


Figure 1.8: HiSPARC data for stations 8001 and 3001 around the epoch of GLE 71 on 17/05/2012. The plot shows the minute-averaged and 5-minute-averaged trigger events between detectors within the station. The vertical red, dashed line depicts the approximate onset time of the GLE. The units of time on the x-axis are, MM-DD HH.

We can see from Figures 1.7, 1.8, and 1.9 there are no clear and obvious signs of the GLE signals in the HiSPARC observations, as was clear for those given in Fig. 1.1 for the Oulu NM station, in Finland. This is the case for both the events data and the singles data.

There are some excursions from the mean count rate which make it difficult to determine variations from space weather events and other sources; this is significantly more prominent in the singles rates which are shown in the GLE 72 plots (Fig. 1.9) for stations 501, 203, and 8001. We believe these excursions are the effect

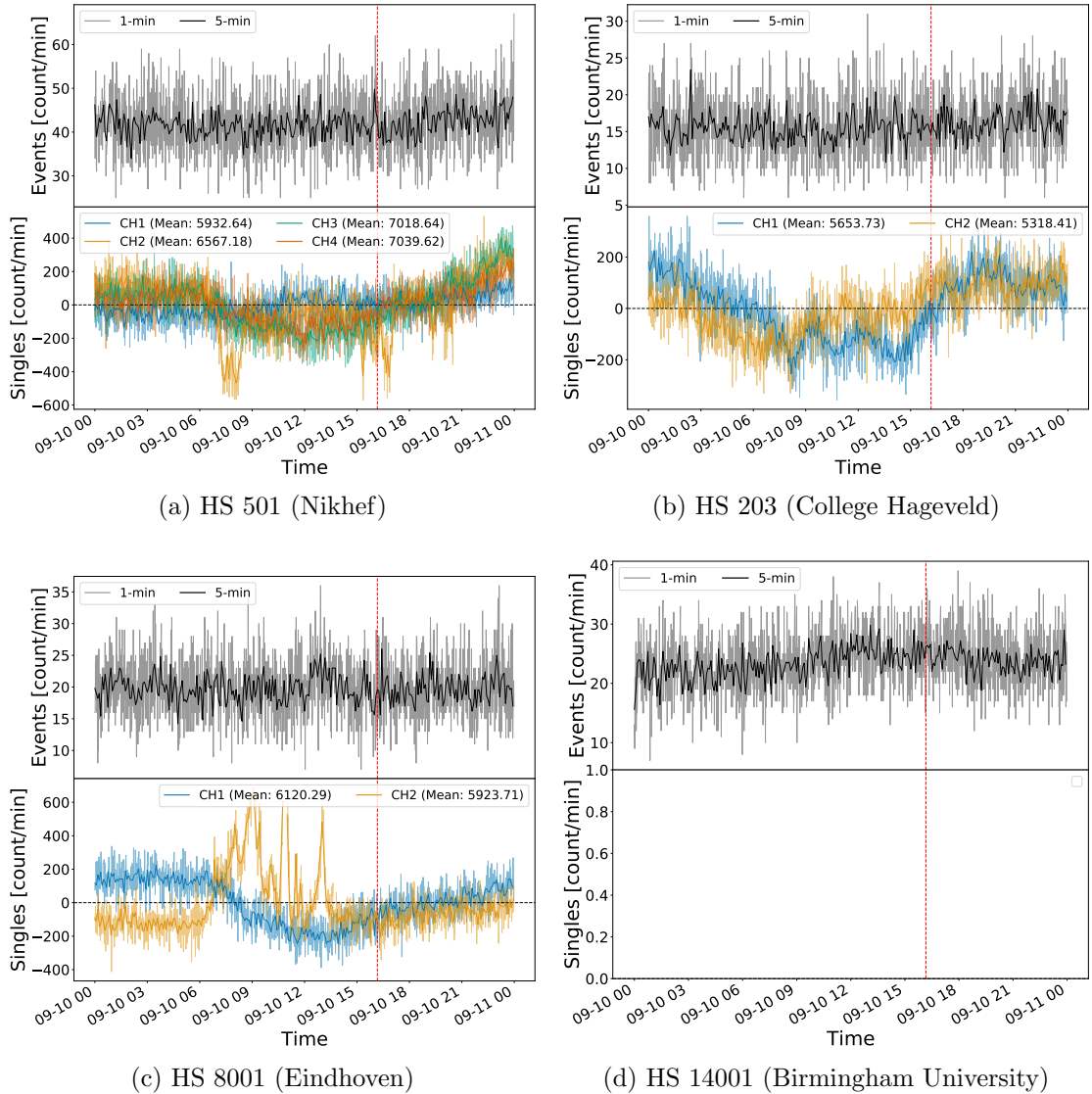


Figure 1.9: HiSPARC data for 4 stations around the epoch of GLE 72 on 10/09/2017. The top panel of each subplot shows the 1- and 5-minute averaged trigger events between detectors within the station, while the bottom panel shows the 1- and 5-minute averaged singles counts, mean-subtracted, for each individual detector (or signal channel,  $CH_n$ ) in the station. The vertical red, dashed line depicts the approximate onset time of the GLE. The units of time on the x-axis are, MM-DD HH.

of atmospheric pressure and temperate on the muon count rates; in Section 1.6 this is discussed further and the effect is accounted for. After its removal we then re-investigated the corrected data, which is discussed in Section 1.7. We also see the existence of a diurnal signal in Figure 1.8a, with CR count rates peaking at around midday. We expect a daily variation from a combination of the CR anisotropy in the interplanetary space and the rotation of the Earth meaning detectors look in dif-

ferent directions over the course of a day. The diurnal variation is expected to have a magnitude of  $< 1\%$  ([Mishra & Mishra, 2007, 2008](#); [Dubey et al., 2016](#); [Thomas et al., 2017](#)), but here we see an increase of  $\sim 50 - 100\%$ , which suggests there may be an additional factor causing the signal.

No clear GLEs have been observed in the HiSPARC data. We believe this is due, in-part, to the rigidity cut-off of the HiSPARC stations, as well as the different particle species observed by HiSPARC compared to the NMAs. However, [Humble J. E. et al. \(2012\)](#) state that NM stations with cut-off rigidities up to  $\sim 15$  GV observed the GLE in September 1989, indicating that SEPs up to at least  $\sim 15$  GeV must have been present in the spectrum during that, particularly large, event. Therefore, the rigidity cut-off of the HiSPARC stations is not necessarily the limiting factor. It is also possible that the PCRs are insufficient to produce EASs of muons, as we know the HiSPARC network is nominally used for observations of UHECRs with energies several orders of magnitude larger.

GLEs are normally associated with SEPs with energies in the MeV to low-GeV regime; hence why typically GLEs are observed by NMAs. Only the most energetic events have been observed by MDs as they are more sensitive to the hard component of the PCR spectrum ([Augusto et al., 2016](#)). Observations of GLEs with HiSPARC will therefore only be linked with the maximum energy release during solar flares, and often this is very short and still the SEPs are of insufficient energy to be detected by MDs ([McCracken et al., 2012](#); [Augusto et al., 2016](#)).

To further understand the impact of SEP energies on the HiSPARC observations, in Section 1.8 we used air shower simulations to investigate the CR spectrum at quiet times and during GLEs.

### 1.5.2 Observations of Forbush Decreases

The search for evidence of FDs within the HiSPARC data was conducted for the FDs highlighted in Table 1.1. Figures 1.10, 1.11, and 1.12 show the HiSPARC

observations around the epochs of the first four FDs listed in Table 1.1. Each of the plots shows only observations using the HiSPARC events data (i.e. coincidences between the detectors of a station), as singles data were not available at those epochs (see Fig. 1.4).

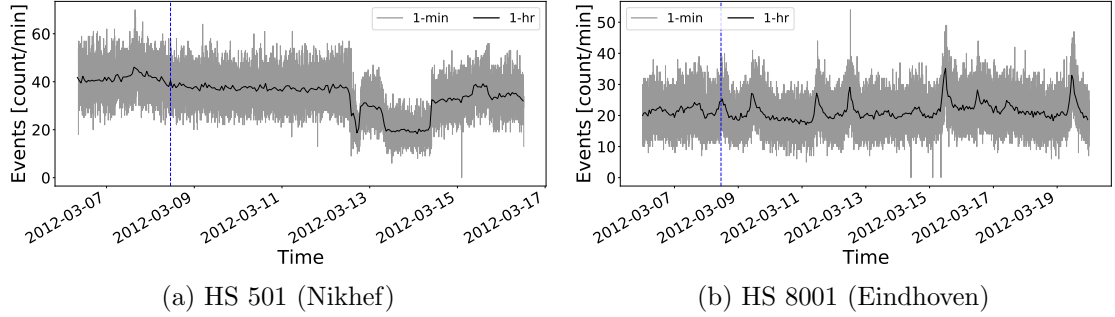


Figure 1.10: HiSPARC data for stations 501 and 8001 around the epoch of the FDs in March 2012. The plot shows the minute-averaged and hourly-averaged trigger events between detectors within the station. The vertical blue-dashed lines show the approximate onset-time of the FDs. The units of time on the x-axis are, YYYY-MM-DD.

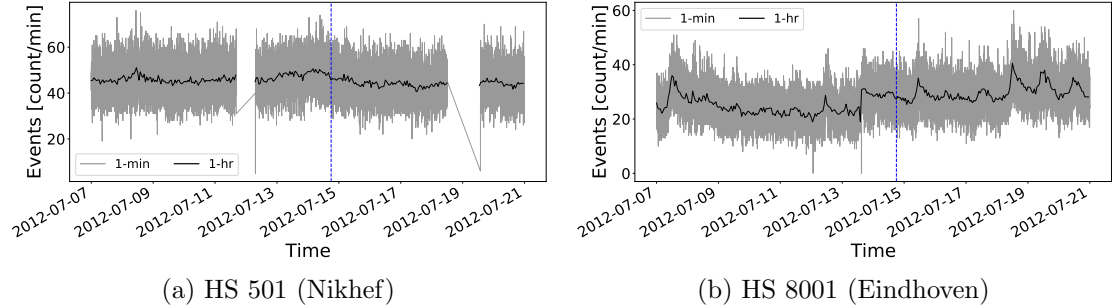


Figure 1.11: HiSPARC data for stations 501 and 8001 around the epoch of the FD in July 2012. The plot shows the minute-averaged and hourly-averaged trigger events between detectors within the station. The vertical blue-dashed line shows the approximate onset-time of the FD. The units of time on the x-axis are, YYYY-MM-DD.

We can see from the plots that there were no clear signs of the FD signals in the HiSPARC data shown here. We observed a set of significant decreases in the muon count rate in station 501 after the second FD in March 2012 (see Figure 1.10a); however, it is unclear whether this was a consequence of the FD or other hardware reasons, as the FD was not observed in the other HiSPARC station. The shape of the FD in the NM data shows a sudden decrease and a smooth recovery within two

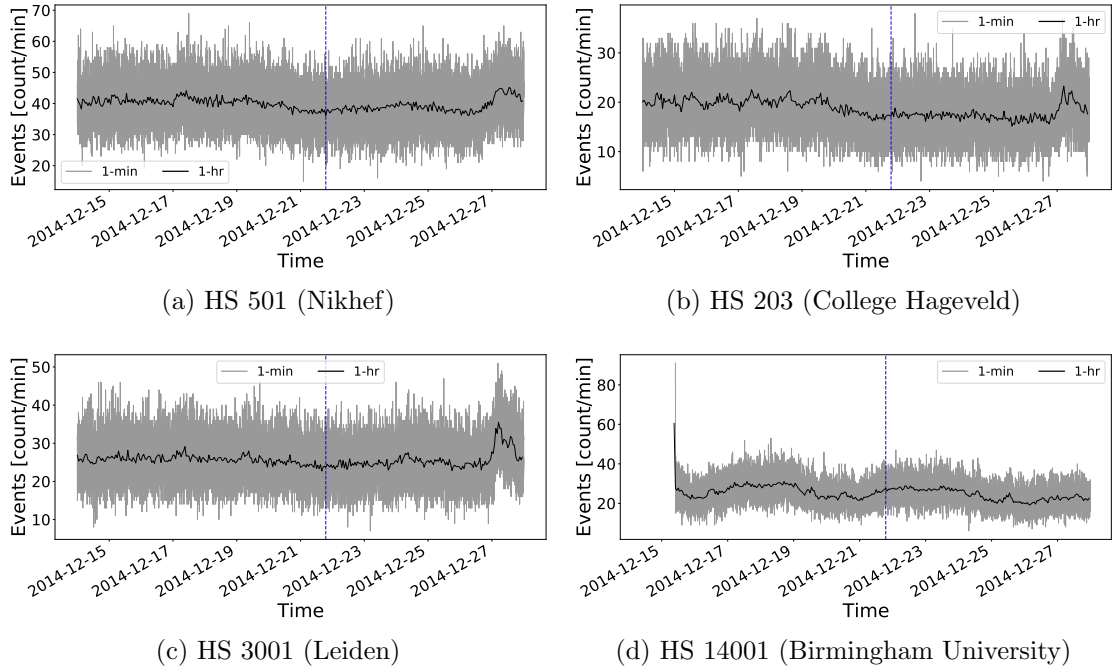


Figure 1.12: HiSPARC data for four stations around the epoch of the FD in December 2014. The plot shows the minute-averaged and hourly-averaged trigger events between detectors within the station. The vertical blue-dashed line shows the approximate onset-time of the FD. The units of time on the x-axis are, YYYY-MM-DD.

days, but the shape of the HiSPARC observations traces a more complex evolution, which suggests that the cause is not the FD, but rather a result of hardware.

As we saw with the earlier investigation into GLEs, we again see excursions from the mean count rate which vary over longer time scales. This is due to variations in the atmospheric pressure. In Section 1.6 this is discussed further and the effect is accounted for.

In addition, it is quite clear from Figure 1.10b and Figure 1.11b that station 8001 (Eindhoven) displays a semi-persistent diurnal variation in the count rate. We know that daily variation is a combination of the CR anisotropy in the interplanetary space and a consequence of the rotation of the Earth meaning detectors look in different directions over the course of a day; however, we typically expect this diurnal variation to be  $< 1\%$  ([Mishra & Mishra, 2007, 2008](#); [Dubey et al., 2016](#); [Thomas et al., 2017](#)), but here we see an increase of  $\sim 100\%$ , which suggests there may be an additional factor due to another source, likely originating in hardware.

For the final two FDs listed in Table 1.1, the plot of the HiSPARC observations is shown in Figure 1.13. Plotted are the HiSPARC events data; however, where possible, we also show the singles rates from each of the individual detectors in a station, when available. Furthermore, as these FDs were precursory to GLE 72, we also marked on the epoch of the GLE for completeness.

As with the other FD epochs, we again do not observe any clear signs of the FD signals in either the events nor singles data. In each of the three stations for which there were singles data, we observed a semi-persistent diurnal signal. This was also seen in the events data for station 14001. In the singles data we a strong diurnal variation of up to  $\sim 50\%$  (see detector channel 2 in Fig. 1.13c). As previously discussed, we expect a diurnal variation of  $< 1\%$ , increasing around local midday ([Mishra & Mishra, 2007, 2008](#); [Dubey et al., 2016](#); [Thomas et al., 2017](#)); however, in Figure 1.13c not only do we see a stronger variation, we also see that the two detectors are anti-correlated, suggested that this signal is a manifestation of thermally induced noise in each detector.

We conclude that no clear signature of FDs has been observed in the HiSPARC data. We again believe this could be linked to the rigidity cut-off of the HiSPARC stations, but also it is possible that the reason originates in the lower sensitivity to lower rigidity PCRs of MDs compared to NMs. We also note that the atmospheric effects in the raw data limit our ability to observe the space weather effects, therefore in the next section we remove these effects to standardise the HiSPARC data.

## 1.6 Atmospheric Corrections of HiSPARC Data

### 1.6.1 Motivation

It is well known that observations made by ground-based CR detectors are susceptible to atmospheric conditions ([Dorman, 2004, 2010](#); [Berkova et al., 2011](#); [De Menonça et al., 2013](#); [Paschalis et al., 2013](#)). As we have seen in the plots shown in Section 1.5, there exist excursions in the data whose origins are from atmospheric

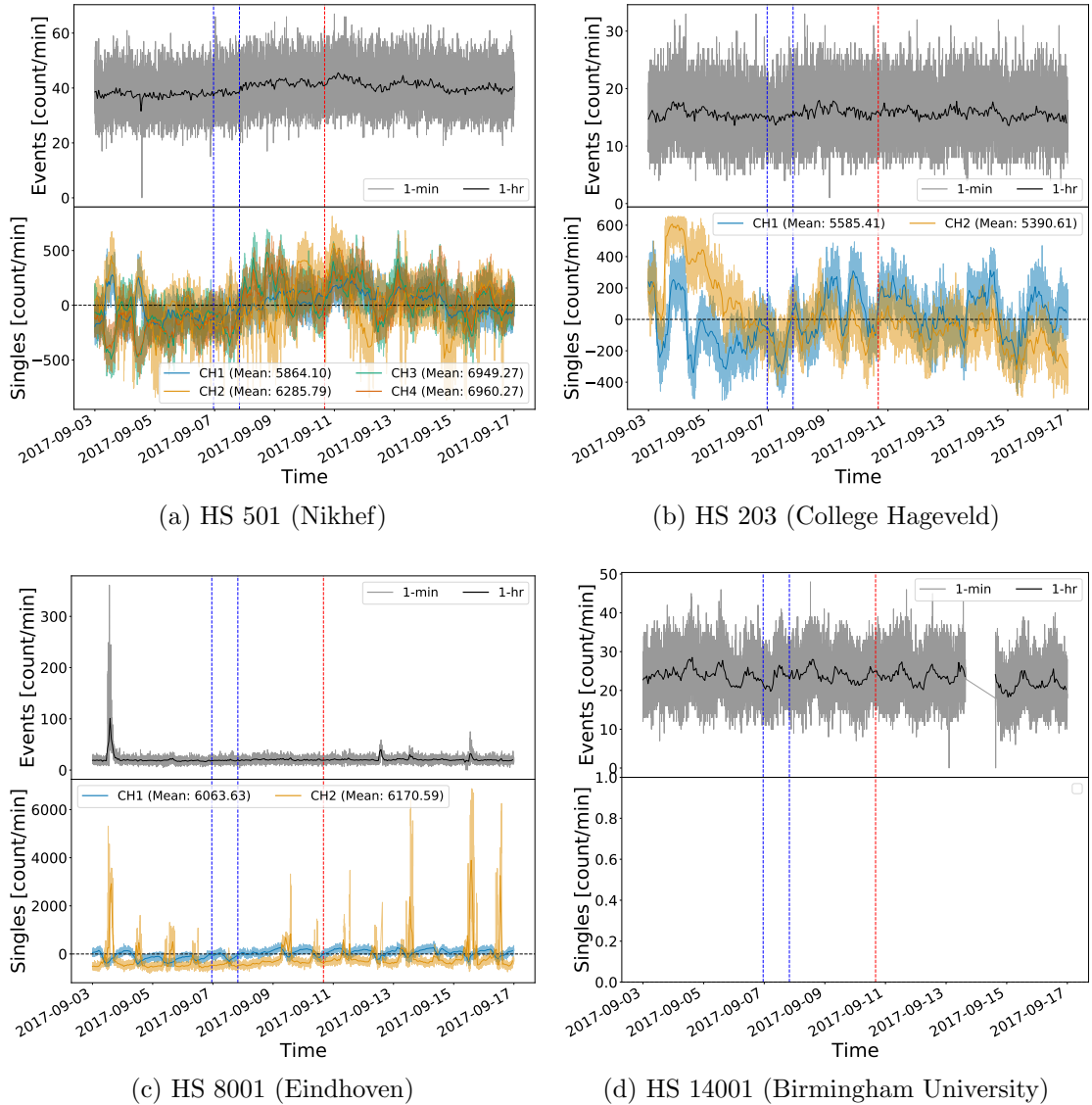


Figure 1.13: HiSPARC data for four stations around the epoch in which there were two FDs close to the onset of GLE 72. The top panel of each subplot shows the minute- and hourly-averaged trigger events between detectors within the station, while the bottom panel shows the minute- and hourly-averaged singles counts, mean-subtracted, for each individual detector (or channel,  $CH_n$ ) in the station. The vertical blue-dashed lines show the approximate onset-times of the two FDs observed around this epoch and the red-dashed line depicts the approximate onset time of the GLE. The units of time on the x-axis are, YYYY-MM-DD.

variations. This sensitivity makes it difficult to differentiate between variations due space weather events and those due to Earth's atmospheric conditions, therefore it was necessary to correct for these effects in the data.

## 1.6.2 Barometric Correction

Atmospheric pressure affects the CR path length due to the expansion and contraction of the atmosphere with varying pressure (Dorman, 1972; Paschalis et al., 2013); hence the CR counts are observed to be negatively correlated to atmospheric pressure as shown for both NM and MDs in Figure 1.14.

A correction for this barometric effect is routinely applied as part of the data calibration for all NM stations within the NMDB and an online barometric coefficient tool<sup>4</sup> is available for NMs, which allows users to perform the barometric correction for a given station over a user-defined epoch (Paschalis et al., 2013). There is no such process routinely applied in the HiSPARC data pipeline.

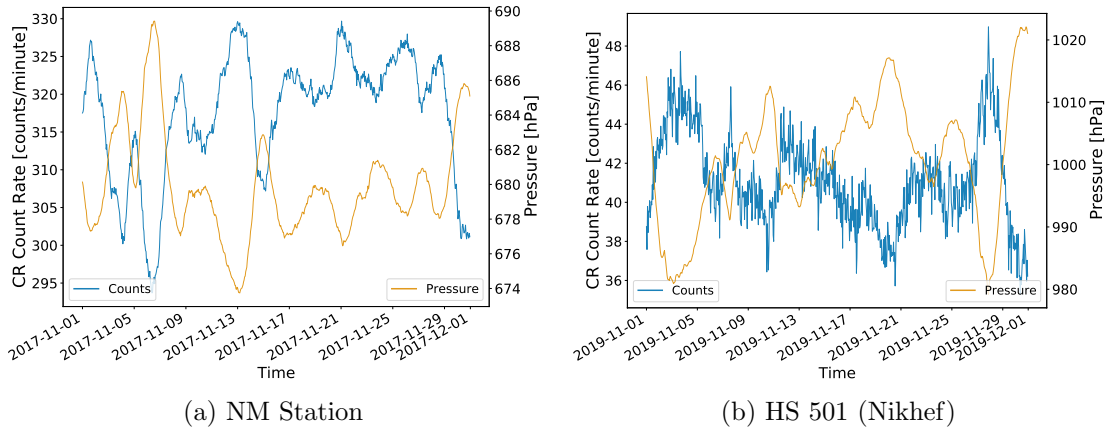


Figure 1.14: The anti-correlation between CR count rates and the atmospheric pressure. (a) shows the CR and the local atmospheric pressure measured at a NM in the South Pole; (b) shows the CR and pressure measured by HiSPARC station 501. In both plots, the data shown is hourly-averaged, to highlight the effects.

The method of correcting for the barometric effect is discussed widely in the literature regarding NMs and is shown to depend on the barometric coefficient (Paschalis et al., 2013). Assuming the cosmic ray flux variation, absent of the atmospheric effects, is reasonably stable, then a simple correction to the counts can be made. The CR variations ( $N$ ) that depend on the local atmospheric pressure are described by:

---

<sup>4</sup><http://cosray.phys.uoa.gr/index.php/data/nm-barometric-coefficient>

$$\Delta N = -\beta N \Delta P, \quad (1.2)$$

where  $\Delta N$  is the change in count rate,  $\beta$  is the barometric coefficient, and  $\Delta P = P - P_0$  is the deviation in pressure from the average ( $P_0$ ) in the given time-period (Paschalis et al., 2013)

Through the integration of equation (1.2), the solution shows the dependence of cosmic ray intensity on pressure,

$$N = N_0 e^{-\beta \Delta P}. \quad (1.3)$$

Therefore by taking the logarithm of equation (1.3), one can obtain the barometric coefficient by fitting the linear model to the observed data, in the form:

$$\ln \left( \frac{N}{N_0} \right) = -\beta \Delta P, \quad (1.4)$$

where  $N_0$  may be considered as the mean count rate over the given time-period of observations.

A demonstration of this method is shown for both a NM and a HiSPARC station in Figure 1.15. In both cases the linear fit does a good job of finding the barometric coefficient and was used to remove the pressure effect from the data.

For comparison, and to show the success of this method at removing the pressure variation, the raw and corrected HiSPARC data are shown in Figure 1.16. It is clear from Figure 1.16 that the large excursions are adequately removed from the data after the correction.

Using the online barometric coefficient tool (Paschalis et al., 2013), it was possible to also provide a comparison between the method used in this work and the correction of the NMDB stations, as a further validation. This is shown in Figure 1.17 for monthly corrections throughout 2017 for the NM station at the South Pole (SOPO).

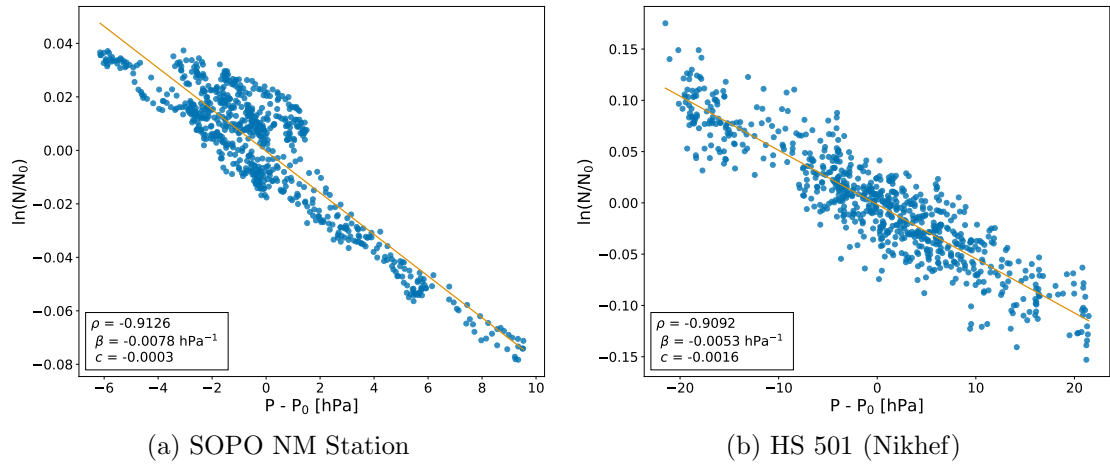


Figure 1.15: The barometric coefficient calculation: (a) during November 2017 for the South Pole (SOPO) NM station, (b) during November 2019 for HiSPARC station 501 at Nikhef.

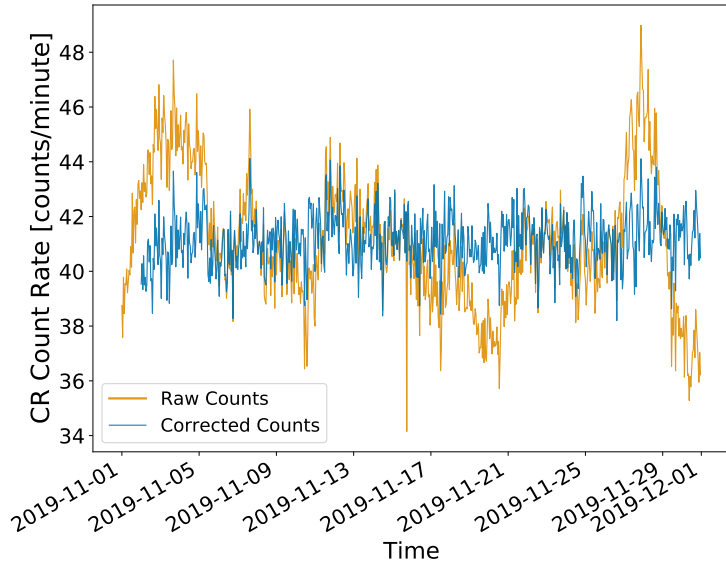


Figure 1.16: A comparison between the hourly-averaged HiSPARC count rate before (orange line) and after the pressure correction (blue line).

Figure 1.17 shows a close agreement between the barometric coefficient calculated in this work and those acquired from the online tool for the SOPO NM. This was also true for other stations tested (Apatity and Rome), thus validating that the method used in this work was suitable for application on the HiSPARC data. The barometric correction was performed on the HiSPARC data for stations where sufficient pressure data and count rates existed.

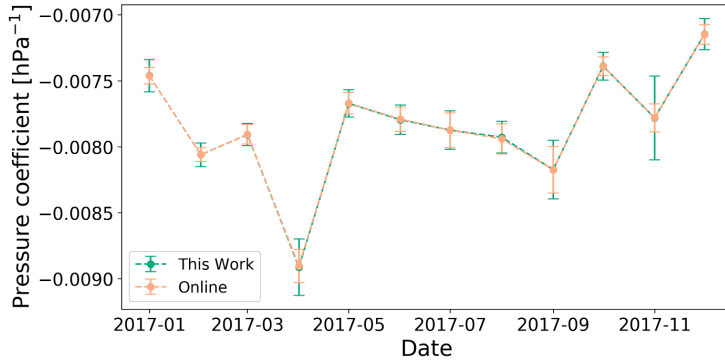


Figure 1.17: A comparison between the monthly barometric coefficient computed in this work and using the online barometric coefficient tool throughout the year 2017 for the SOPO NM station.

### 1.6.3 Temperature Correction

The effects of atmospheric temperature have been shown to influence both the creation and disintegration processes for muons in the atmosphere (Berkova et al., 2011). There is hence a positive effect and a negative effect on muon intensity as a consequence of temperature variations (Mendonça et al., 2016).

The positive effect is related to pion decay and its dependence on temperature variation. The higher the temperature, the lower the atmospheric pion absorption, which implies a higher generation rate of muons (Mendonça et al., 2016).

The negative effect corresponds to the decrease of muon intensity at ground level as the muon average path length varies with temperature. Due to the heating and expansion of the atmosphere during summer periods muons are produced higher in the atmosphere; hence the muon propagation path length increases meaning there is more atmosphere for muons to traverse before reaching the ground, and an increased decay probability and ionisation losses (Savić et al., 2015; Mendonça et al., 2016).

Due to the difference in decay probability, the negative effect dominates for low energy muons and the positive effect dominates for high energy muons (Berkova et al., 2011). It is therefore expected that the negative effect should dominate for the HiSPARC network. This is in contradiction with the observations of diurnal variation with the HiSPARC detectors, as one can quite clearly see that the HiSPARC

stations register higher count rates during local noon (see Fig. 1.9c). However, when observing the singles rates, we do see some detectors displaying a positive effect and some displaying a negative effect (see Fig. 1.9). This is not consistent between stations, and provides more evidence to suggest this is an effect of thermally induced noise in the Photo Multiplier Tubes (PMTs).

Several methods of correcting for the temperature effect are discussed in the literature, see [Berkova et al. \(2011\)](#); [Mendonça et al. \(2016\)](#) for a summary. However, the methods discussed are typically applied over long timescales of years, to account for seasonal variations with low temporal resolution, rather than to account for short timescale variations with periods of less than a day; hence these methods aren't necessarily suitable for this work on ephemeral space weather events.

The HiSPARC stations provide the local outdoor temperature which is measured nearby the detectors and also the temperature in the room where the electronics are located. The latter is not of use, but the former can be used for temperature corrections. Figure 1.18a shows the pressure corrected events data and the temperature data for station 8001 in July 2012. There is a strong correlation between the events and the temperature, which is demonstrated in Figure 1.18b, yet weaker than with pressure.

We simplified the correction method and used a linear fitting technique (i.e. the same as the barometric correction in Section 1.6.2; however, replacing the pressure for locally measured outdoor temperature). We can see from Figure 1.19 that this correction method does remove a significant amount of the variation correlated with the outdoor variation, including dampening the strong diurnal variation. There still persists some strong variation in the count rate however, which shows that this method is not as effective as the pressure correction. Nevertheless, we continue with this temperature correction as it is sufficient at reducing the diurnal variation in the data around the events considered.

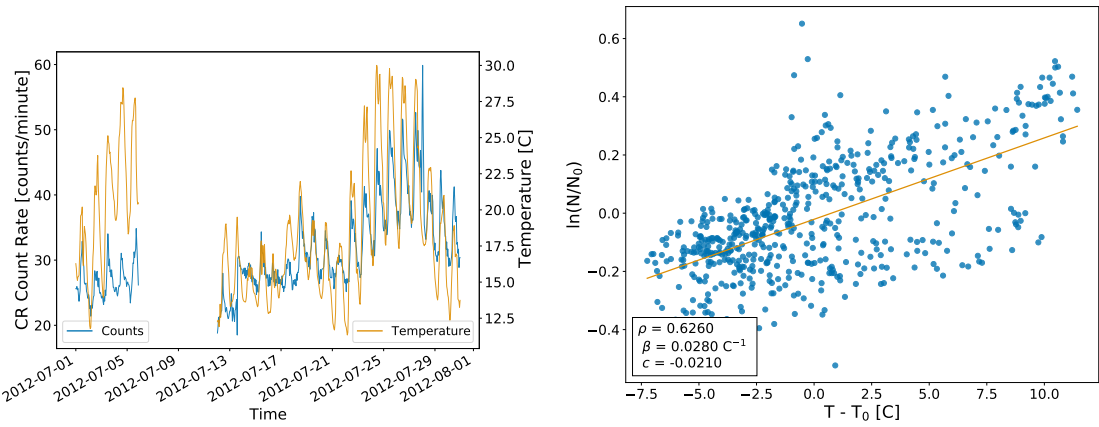


Figure 1.18: The relationship between the pressure corrected events data and the outdoor temperature as measured at HiSPARC station 8001 (Eindhoven). (a) shows the time-series of hourly-averaged pressure corrected events and temperature data; (b) shows the correlation between the counts and temperature, and the fitted line to calculate the correction coefficient.

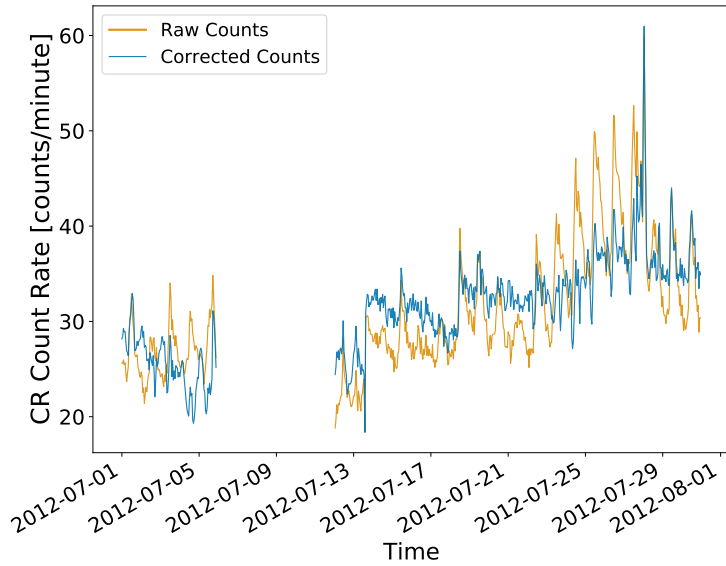


Figure 1.19: A comparison between the hourly-averaged HiSPARC count rate before (orange line) and after the temperature correction (blue line). After the correction, the diurnal variation from the temperature effect has been reduced.

## 1.7 HiSPARC Observations After Atmospheric Corrections

### 1.7.1 Observations of Ground Level Enhancements

Following the atmospheric correction, the search for evidence of GLEs was re-conducted, this time within the corrected HiSPARC data. This could only be done for GLE 71 and 72, as the HiSPARC network was not collecting meteorological data during the epoch of GLE 70. Figure 1.20 and Figure 1.21 show the atmospheric-effect corrected HiSPARC observations around the epochs of GLE 71 and 72, respectively. The observations of GLE 71 show only the HiSPARC events data; however, we also show the singles rates from each of the individual detectors in a station for GLE 72.

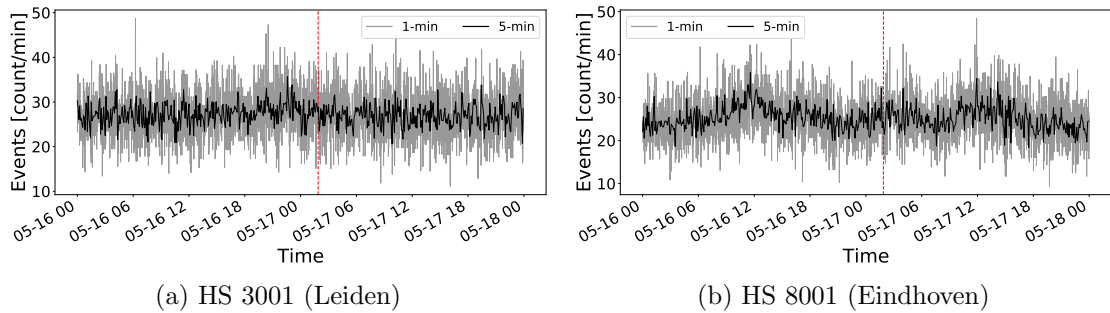


Figure 1.20: Atmospheric-corrected HiSPARC data for stations 8001 and 3001 around the epoch of GLE 71 on 17/05/2012. The plot shows the minute-averaged and 5-minute-averaged trigger events between detectors within the station. The vertical red, dashed line depicts the approximate onset time of the GLE. The units of time on the x-axis are, MM-DD HH.

Despite the atmospheric correction, in general, doing a good job at removing atmospheric variations in the CR counts, there still remained no clear GLEs observations in the pressure corrected HiSPARC data. We believe this is due to a mixture of the reasons discussed above. A high rigidity cut-off of the HiSPARC stations leads to a low increase in the CR count, as GLEs are typically caused by SEPs with a lower energy; hence too few additional muons were produced during the GLEs. Again we should however note that [Humble J. E. et al. \(2012\)](#) stated that

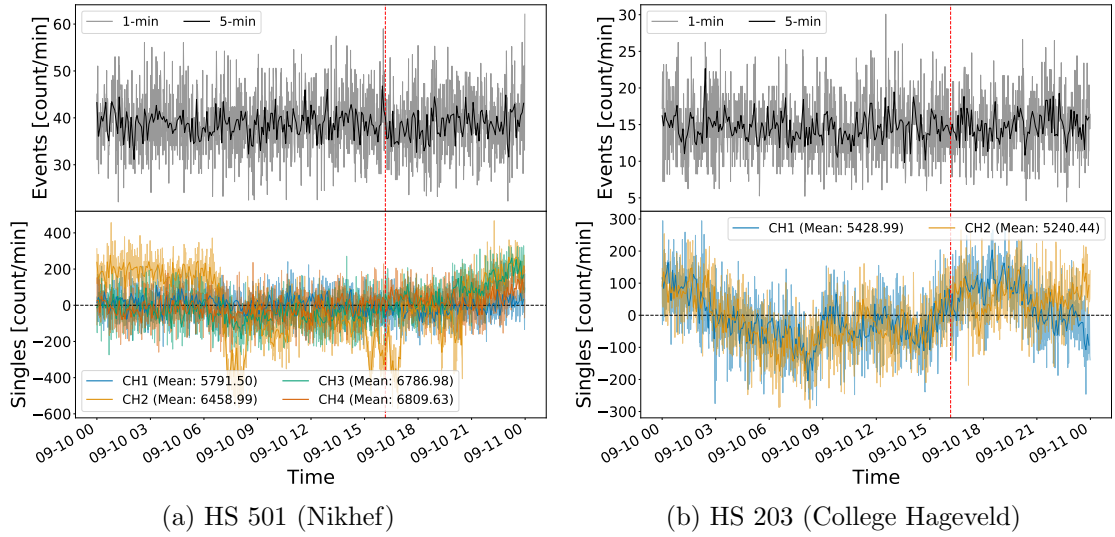


Figure 1.21: Atmospheric-corrected HiSPARC data for 2 stations around the epoch of GLE 72 on 10/09/2017. The top panel of each subplot shows the 1- and 5-minute averaged trigger events between detectors within the station, while the bottom panel shows the 1- and 5-minute averaged singles counts, mean-subtracted, for each individual detector (or signal channel,  $CH_n$ ) in the station. The vertical red, dashed line depicts the approximate onset time of the GLE. The units of time on the x-axis are, MM-DD HH.

NM stations with cut-off rigidities up to  $\sim 15$  GV observed the GLE in September 1989, indicating that high-energy SEPs may be present and also cause GLEs, suggesting the rigidity cut-off may not be the limiting factor. In addition, as discussed above, the events data require a trigger between 2 detectors that are separated by up to 10 m, therefore this further biases the stations to be sensitive to more energetic PCRs. Furthermore, the issue could be due to the particle species, re-emphasising the wide use of NMs instead of MDs.

This provides motivation to investigate the flux of muons at ground level during quiet periods, i.e. from GCRs, compared to the flux of muons at ground level during energetic solar events such as GLEs. This work was performed and is discussed in Section 1.8.

### 1.7.2 Observations of Forbush Decreases

The search for evidence of FDs was also re-conducted using the atmospheric-effect corrected HiSPARC data. Figure 1.22 and Figure 1.23 shows the corrected HiS-

PARC observations around the epochs of a FD in July 2012 and December 2014, respectively.

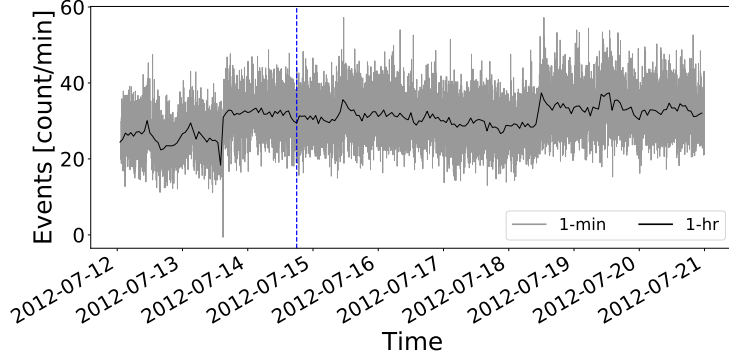


Figure 1.22: Atmospheric-corrected HiSPARC data for station 8001 (Eindhoven) around the epoch of the FD in July 2012. The plot shows the minute- and hourly-averaged trigger events between detectors within the station. The vertical blue, dashed line depicts the approximate onset time of the FD. The units of time on the x-axis are, YYYY-MM-DD.

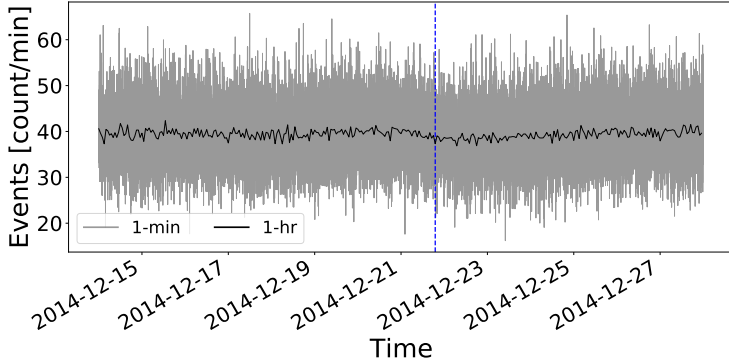


Figure 1.23: Atmospheric-corrected HiSPARC data for station 501 (Nikhef) around the epoch of the FD in December 2014. The plot shows the minute- and hourly-averaged trigger events between detectors within the station. The vertical blue, dashed line depicts the approximate onset time of the FD. The units of time on the x-axis are, YYYY-MM-DD.

In Figure 1.22 there are no clear FD observations in the corrected HiSPARC data; however, in Figure 1.23 there is a slight indication of a  $\sim 2\%$  decrease in the count rate at the epoch of the expected FD. This suggests that after correcting the data for atmospheric effects, that FDs on the order of  $\sim 2\%$  may be observed by the HiSPARC network.

Finally, the atmospheric-effects corrected observations of the two FDs which occurred around GLE 72 is shown in Figure 1.24, showing the corrected events data

and singles data for each of the individual detectors in the stations.

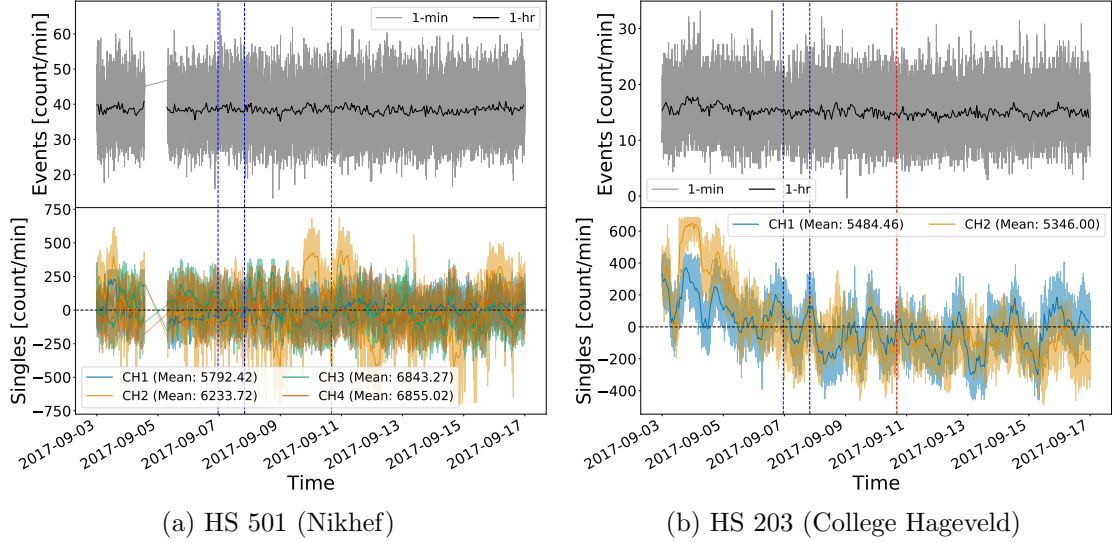


Figure 1.24: Atmospheric-corrected HiSPARC data for 2 stations in an epoch where there were two FDs close to the onset of GLE 72. The top panel of each subplot shows the minute- and hourly-averaged trigger events. The bottom panel shows the minute- and hourly-averaged singles counts, mean-subtracted, for each individual detector (or signal channel,  $CH_n$ ) in the station. The vertical blue-dashed lines show the approximate onset-times of the FDs and the red-dashed line depicts the approximate onset-time of the GLE. The units of time on the x-axis are, YYYY-MM-DD.

There are no clear FDs in Figure 1.24, and the singles plots demonstrate that the atmospheric corrections do not sufficiently remove all the signal excursions from the mean, and there remain large (up to 10%) deviations in the signals. One reason for this, particularly for the singles, is that the measured temperature is recorded in the atmosphere and not inside the roof boxes containing the PMTs. The roof boxes are made of plastic and one would suspect the air temperature inside the boxes is different to the ambient atmospheric temperature measured nearby. In order to fully remove the effects of thermally induced count variations, we must record the more accurate temperatures of the PMTs instead of just the atmospheric temperature.

## 1.8 Air Shower Simulations

### 1.8.1 Motivation

There is no evidence to suggest the GLEs were observed in the HiSPARC data, even after correcting for atmospheric effects of pressure and temperature. This leads us to question whether it is possible to observe GLEs with the HiSPARC detectors. In order to answer this, we needed to understand the muon flux at ground level and the scale of air shower muon footprints produced by PCRs. To investigate this, simulations of air shower development were performed for a range of PCRs energies for both primary protons and  $\alpha$ -particles.

To simulate the CR air shower development, the Cosmic Ray Simulations for Kascade (CORSIKA) software was employed: a Monte Carlo programme providing detailed simulations of the evolution of air showers initiated by PCRs through the atmosphere ([Heck & Pierog, 2017](#)). The particles in the CORSIKA simulations are tracked through the atmosphere until they undergo interactions with atmospheric nuclei, decay due to their instability, or reach the ground level defined as the simulation terminator.

Proton and  $\alpha$ -particle initiated air showers were generated with energies ranging from  $10^9$ – $10^{20}$  eV, and  $4 \times 10^9$ – $10^{20}$  eV, respectively. In total  $\sim 2 \times 10^5$  proton-initiated showers were simulated and  $\sim 2 \times 10^5$   $\alpha$ -particle-initiated air showers were simulated. Lists detailing the breakdown of PCR energies and number of simulations is provided in Appendix A, along with a brief discussion of the settings chosen within the simulations.

### 1.8.2 Air Shower Footprints

The average footprint of the muons at ground level, due to PCRs, was calculated from the output of the CORSIKA simulations. This was achieved by taking the distribution of the number of muons at ground level at the end of the simulations

as a function of their radial distance from the shower core, as this distance was provided as an output from the simulations. Multiple realisations of the air showers were simulated (see Table A.1). For a given PCR energy, the mean distribution of radial footprints was calculated by averaging over all of the individual simulations. Figure 1.25 shows the radial distribution of muons at ground level for air showers induced by vertically incident protons and  $\alpha$ -particles.

In addition to the vertically induced air showers, we also repeated the simulations for air showers randomly selected from a uniform distribution of incident angles between  $0^\circ$  (vertical) and  $70^\circ$ , to provide a simulation that is more physically representative of CRs arriving from all directions. Radial distributions of muons were produced, similar to those in Figure 1.25, but they are not shown here as the difference is not drastically different by-eye.

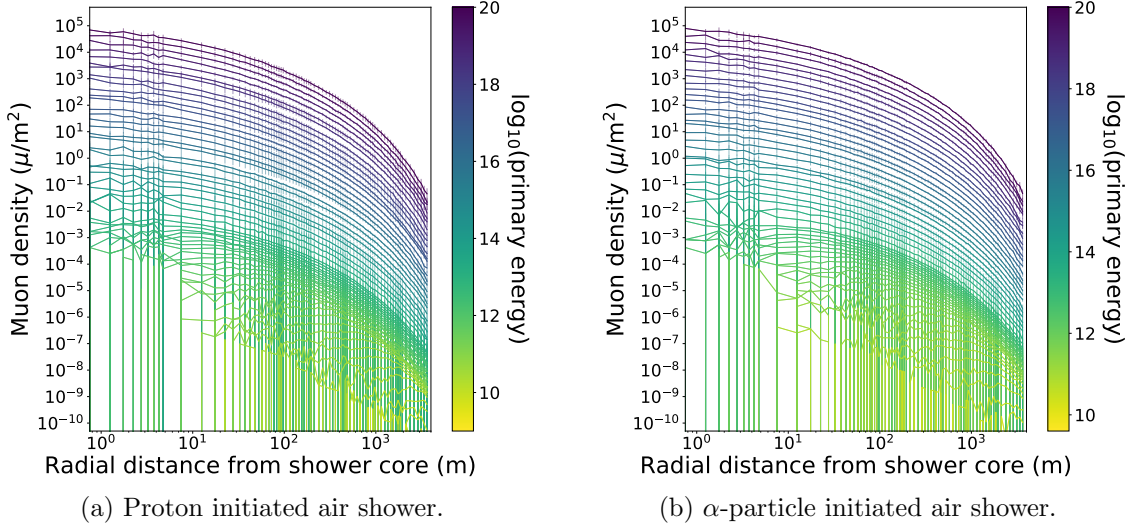


Figure 1.25: Mean muon density footprints for (a) proton-initiated air showers and (b)  $\alpha$ -particle-initiated air showers with initial PCR trajectories with zenith angles  $\theta = 0^\circ$  and various PCR energies. The error bars given represent  $1\sigma$ .

The interpretation of Figure 1.25 provides an understanding of the minimum energy PCRs observable by the HiSPARC network. The typical separation between the detectors in a HiSPARC station is  $\sim 10$  m; however, the separation between detectors varies from station-to-station and can be up to as much as 20 m or as low

as just a couple of metres. The simulations show, to trigger two HiSPARC detectors separated by  $\sim 10$  m by muons from the same shower, the density of the shower needs to be at least  $\sim 0.005 \mu\text{m}^{-2}$ , suggesting that HiSPARC stations typically observe PCRs with a minimum energy on the order of  $\sim 10^{13} - 10^{14}$  eV, which agrees with what was found by [van Dam et al. \(2020\)](#).

This helps to explain why the GLEs and FDs were not observed in the HiSPARC events data. The effects of GLEs and FDs are more prominent at lower PCR rigidities ([Belov et al., 2005](#)) and we showed here the air showers induced by these particles are not sufficient to induce an air shower that will trigger multiple detectors in a station. We see that lower energy PCRs do not produce EASs, but rather a very diffuse scattering of muons reach ground level. It is therefore clearer why we did not observe any GLEs in the events data, as the SEP-induced muons are insufficiently spread to trigger multiple detectors in coincidence. It would have been more likely to have observed GLEs in the singles data, as this only records the count rate of an individual detector, which has been shown to have a high muon-detection efficiency close to 100% ([van Dam et al., 2020](#)). However, again the space weather events were not observed in the HiSPARC singles data, which may be further explained by instead investigating the flux of muons at ground level.

### 1.8.3 Muon Flux

Another output from the CORSIKA simulations was the energy of the muons that reach ground level. From the air shower simulations it was therefore possible to compute an estimate of the energy distribution of muons produced per PCR. Figure 1.26 shows the energy distribution of muons produced per primary PCR, for air showers induced by vertically incident protons and  $\alpha$ -particles.

The vertically incident air showers provides an upper boundary on the muon flux, but we also repeated the simulations for air showers randomly selected from a uniform distribution of incident angles between  $0^\circ$  (vertical) and  $70^\circ$ , to provide

a more physically representative flux. Similar plots were produced to those in Figure 1.26, but they are not shown here, as the difference is not drastically different by-eye.

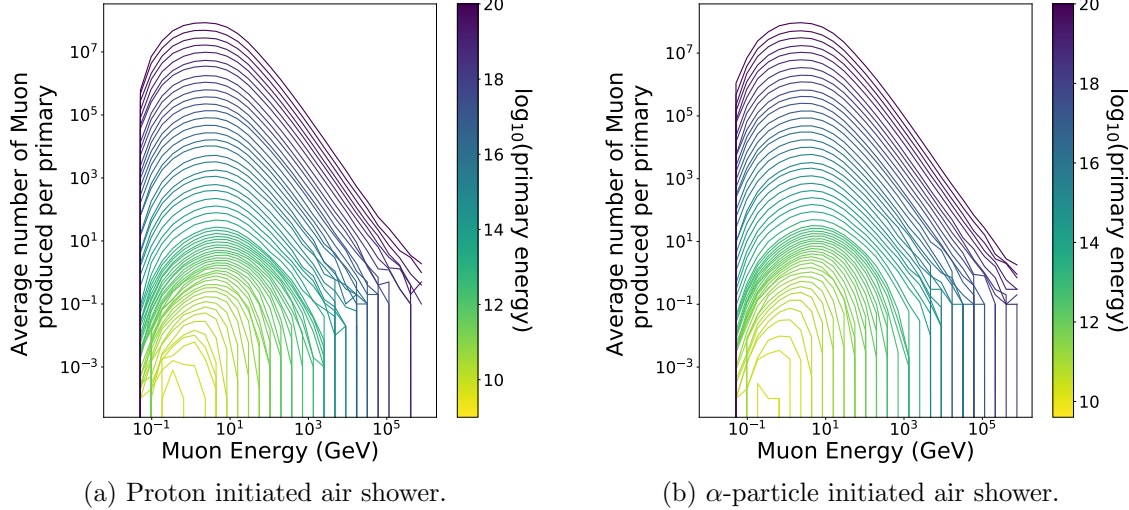


Figure 1.26: Mean number of muons produced at ground level by the PCR for (a) proton-initiated air showers and (b)  $\alpha$ -particle-initiated air showers, for various PCR energies.

We see from this analysis that PCRs with an energy less than  $\sim 10^{11} - 10^{12}$  eV produce on the order of only one muon that reaches ground level, and below this energy it is rare that any muons arrive at ground level. Knowing the effects of GLEs and FDs are more prominent at lower PCR rigidities ([Belov et al., 2005](#)), i.e. energies  $< 10^9$  eV, this helps explain why the space weather events were not observed in the HiSPARC events data. The air showers induced by the lower rigidity PCRs are insufficient to produce significant variations in the flux of the muons at ground level, thus we do not observe a variation from the typical SEPs that induce GLEs.

We also used the data from the simulations to estimate the total muon flux at ground level, based on the PCR flux at the top of the atmosphere. We used a model for the GCR flux at Solar Maximum ([Corti et al., 2019](#)), which utilised measurements from the Alpha Magnetic Spectrometer (AMS-02) on-board the International Space Station (ISS) to estimate the flux of PCRs at the top of the atmosphere. Fig-

Figure 1.27 shows the computed differential flux of muons at ground level, based on the simulations of vertically incident PCRs and those randomly simulated within a  $70^\circ$  acceptance cone. From Figure 1.27, we see that the ground-based flux is similar for both types of simulation performed. In both, the low-energy muon flux dominates, and peak at a muon energy of  $\sim 1$  GeV.

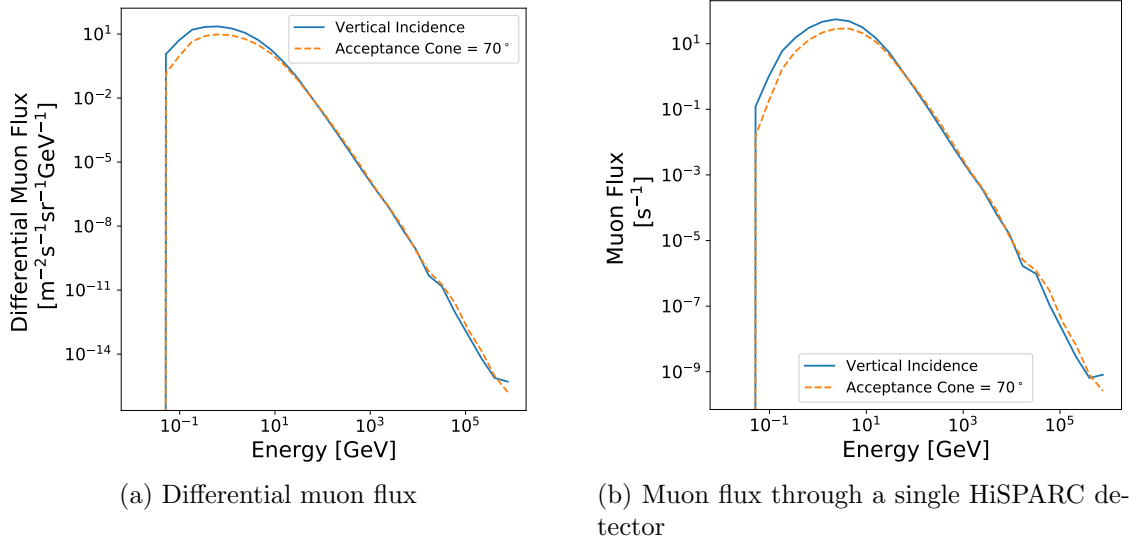


Figure 1.27: Ground level muon spectra as computed in the CORSIKA simulations. (a) shows the differential muon flux at ground level; (b) shows the muon flux through a single HiSPARC detector. In both plots the solid, blue line shows the simulations using vertically incident PCRs, and the dashed, orange line shows the simulations using PCRs incident within a cone of  $70^\circ$ .

The calculated spectra were used to determine the expected rate of muons passing through a single HiSPARC detector. We computed the rates:  $\sim 85 \mu/\text{s}$  (for non-vertical, i.e.  $70^\circ$  acceptance cone simulations), and  $160 \mu/\text{s}$  (for vertical simulations). These rates are comparable to the generally accepted, average ground level muon flux on the order of  $\sim 70 \text{ m}^{-2} \text{ s}^{-1} \text{ sr}^{-1}$  ([Cecchini & Sioli, 2000](#); [Blackmore et al., 2015](#); [Pereira et al., 2020](#); [Zyla, P. A. \(Particle Data Group\) et al., 2020](#)), or  $1 \mu \text{cm}^{-2} \text{ min}^{-1}$  ([Zyla, P. A. \(Particle Data Group\) et al., 2020](#)).

To understand, from the CORSIKA simulations, how the count rate changed during a GLE, the PCR spectrum during the space weather events is needed. Unfortunately this information was not so easily acquired; however, there is a tool

which provided muon fluxes based on the GCR spectrum and also GLE spectra, which is described in the next section.

#### 1.8.4 Muon Flux From MAIRE

As a further comparison, to investigate how the muon flux varied during GLEs we used the online Model for Atmospheric Ionising Radiation Effects (MAIRE) tool to compute the muon spectrum at ground level. MAIRE allows the computation of the secondary particle spectra in the atmosphere, caused by SEPs, including the ground level neutron and muon fluxes. MAIRE has an advantage of also having the PCR spectra for a number of GLEs built-in; however, they are for the strongest GLEs to-date. The GLEs within the MAIRE tool are detailed in Table 1.3, also providing an estimate for the maximum increase in count rate, as observed in the NMDB, as a reference.

Table 1.3: The seven GLEs where MAIRE muon spectra were available, and the maximum observed increase in the neutron flux in the NMDB and the station where the increase was observed.

GLE	Date	Max. % change (station)
5	23/02/1956	~ 5100% (Leeds)
42	29/29/1989	~ 340% (Calgary)
43	19/10/1989	~ 90% (South Pole)
44	22/10/1989	~ 190% (McMurdo)
45	24/10/1989	~ 200% (South Pole)
59	14/07/2000	~ 60% (South Pole)
60	15/04/2001	~ 220% (South Pole)

The GLEs incorporated in the MAIRE tool predate the existence of the HiSPARC network; as a result, the simulations are not directly informative on the GLEs we were investigating in Table 1.1. Nevertheless, the MAIRE simulations helped in our understanding of whether it was likely or possible to observe a GLE using data acquired by the HiSPARC network.

We first used the MAIRE tool to simulate the spectra for the background GCRs and the seven GLEs at the Nikhef (501) HiSPARC station. Figure 1.28 shows the

muon spectra for the GCR spectrum at solar minimum, and the additional muon spectrum for seven of the largest GLEs to date (which are additive to the GCR spectrum).

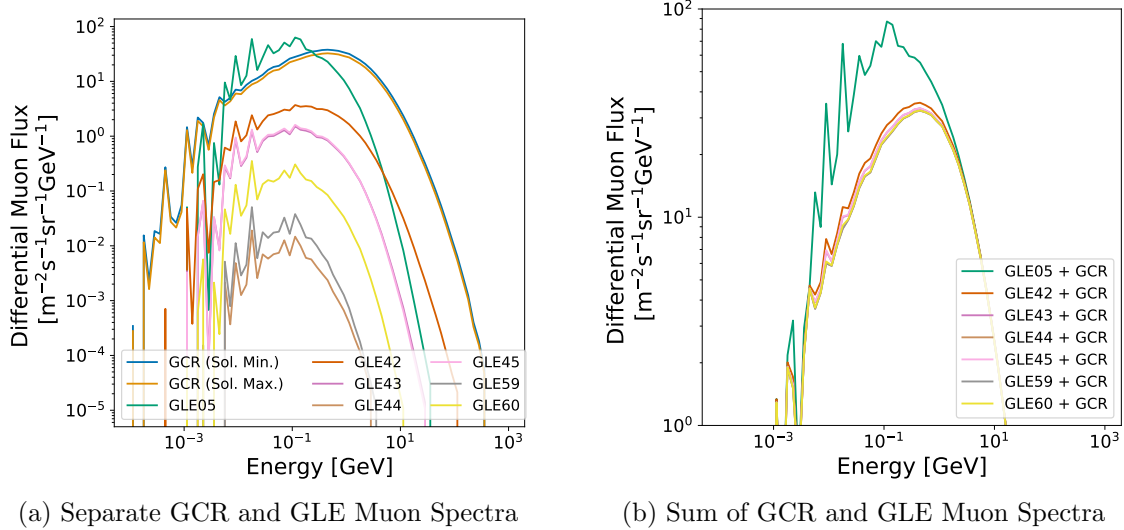


Figure 1.28: Plots of the calculated MAIRE muon spectra for different incident PCR spectra. Blue and orange lines show muon spectra calculated for the incident GCR spectra during solar minimum and maximum, respectively. The other coloured lines show the computed muon spectra for the incident GLE spectra. (a) shows the individual muon spectra for GCRs and GLEs; (b) shows the combined muon spectra for the GCR at solar maximum and the GLEs.

The GCR-induced muon spectrum in Figure 1.28 roughly agrees with that computed using CORSIKA, which gave us confidence in the results of both simulations. We can see that the effect on the muon spectrum drastically varies for the seven GLEs, with GLE 5 clearly the largest event.

Prior to inferring any conclusions about the muon spectra at the HiSPARC stations, as the MAIRE tool provides the neutron flux, we verified the accuracy of the MAIRE results by comparing the observed increases in NM count rates to those predicted by MAIRE. To reduce any effects of strong anisotropy, when comparing to HiSPARC, we chose to analyse the NM count rate at a mid-latitude station, Kiel, which is located in Germany and is one of the nearest NM to the HiSPARC network, at  $\sim 825$  km away. The properties of the Kiel station are:  $R_C=2.36$  GV, Altitude=54 m, Latitude=54.34°N, Longitude=10.12°E ([NMDB, 2018](#)).

Table 1.4 shows a comparison between the observed neutron count increase, measured using data from the NMDB, and the increases predicted by MAIRE. The Kiel NM station was not online in 1956, during GLE 5, therefore this event has been omitted from these results. The MAIRE increases were calculated by comparing the integrated GLE flux to the integrated background GCR flux at that epoch, including the effects of the disturbances in the Earth’s magnetic field from the planetary K-index ( $K_p$ ). The muon count rate increases predicted by MAIRE are also shown in Table 1.4, for comparison.

Table 1.4: Observed and predicted increases in the CR count rates at the Kiel NM station. The observed neutron increases use data from the NMDB, where the errors are the measurement uncertainty from the 5-minute averaged data. The predicted data for the neutrons and muons are from the MAIRE simulations. The ratio column provides a conversion factor from the MAIRE predicted neutron increases compared to those observed. The fraction column shows the proportion of the MAIRE predicted muon increase compared to the MAIRE predicted neutron increase.

GLE	Neutron Increase			Muons Increase	
	Observed	Predicted	Ratio	Predicted	Fraction
5	-	-	-	-	-
42	$\sim 160 \pm 5\%$	88.7%	1.80	3.98%	4.45%
43	$\sim 19 \pm 1\%$	59.6%	0.32	0.790%	1.32%
44	$\sim 6 \pm 1\%$	2.6%	2.30	0.00376%	0.14%
45	$\sim 45 \pm 2\%$	67.9%	0.66	0.817%	1.20%
59	$\sim 8 \pm 1\%$	6.1%	1.32	0.00906%	0.15%
60	$\sim 24 \pm 2\%$	18.8%	1.28	0.0814%	0.43%

We can see from Table 1.4 that there is a stark contrast between the observed NM increase and that predicted by MAIRE. One possible cause is inaccuracy in the predictions; however, this is unlikely as [Lei et al. \(2004\)](#) have shown the verification of their results versus observations. More likely, the difference is due to the anisotropy of the CRs initiating the GLEs, as MAIRE does not adequately account for anisotropy in the simulations ([Dyer et al., 2003](#); [Lei et al., 2004](#)). The ranked ordering from strongest to weakest GLEs in the observed Kiel data and that predicted by MAIRE are in good agreement, suggesting that despite an incorrect amplitude of the increase, generally the two data sets agree on which GLEs were the

strongest. The ratio column gives a factor to convert from the MAIRE predicted increase to the NMDB observed increase. This was used as a calibration factor, to ensure agreement between the MAIRE predictions and the observed data. Furthermore, as the ratio provides us with a calibration to recover the observed increase in neutron counts from the MAIRE simulations, we assumed the same calibration factor may be applied to the predicted increase in the muon counts. This conversion is shown in Table 1.5.

In addition, comparing the fraction of the predicted muon to neutron increase shown in Table 1.4, we see the significantly reduced prediction for the muon count increase. We know this is due to the energy spectrum of the PCRs, but the values in Table 1.4 provides a quantitative estimate of this and serves as further evidence to show that we may be unable to observe weaker GLEs with the HiSPARC network.

We calculated the increase in muon count rate at several HiSPARC stations, and the predicted rates were adjusted by the ratio factor in Table 1.4. These calculations relied on the assumption that the anisotropy does not have a significant effect on the increase observed between the Kiel NM station, and the HiSPARC stations in the Netherlands and the UK. The predicted count rates, adjusted for the factors in Table 1.4, are shown in Table 1.5. Again, GLE 5 has been omitted from these results as the Kiel station was not online then, so we cannot calibrate the MAIRE predictions.

Table 1.5: The MAIRE predicted increase in the muon flux, adjusted for the calibration factor between observed and predicted neutron increases at the Kiel station, in Table 1.4.

GLE	Predicted Muon Increase		
	Kiel	HS 501	HS 14001
5	-	-	-
42	7.18%	7.15%	7.33%
43	1.42%	1.40%	1.47%
44	0.00678%	0.00435%	0.00550%
45	1.47%	1.44%	1.53%
59	0.0163%	0.0102%	0.0123%
60	0.147%	0.139%	0.146%

The predicted increase in the muon count rates, calculated using the MAIRE simulations, for the NM station and the HiSPARC stations, in both the Netherlands and the UK, are in near-agreement. Assuming the effects of anisotropy are small, this suggests that the predicted spectra at the HiSPARC stations (adjusted for the calibration factor) are representative of the approximate increase one would expect to observe.

The effect of the GLEs shows only a small increase in the muon count rate, and for most of the events induces an increase of  $< 2\%$  in the ground-level muon flux. Furthermore, for the weaker, more frequent standard of GLEs an increase of  $\ll 1\%$  was predicted. The exception in these events is GLE 42. We expect that we would have seen the increase in the HiSPARC data for GLE 42, but it pre-dates the HiSPARC project and thus it cannot be verified. We expect the same would have been true also for GLE 5, but we do not have the Kiel data to form the calibration, to predict the increase. GLE 5 was an exceptionally large event, for which we haven't seen anything similar in over half a decade. Such events are rare, and we expect that the energies involved would have shown a significant increase in the HiSPARC count rate.

These simulations, combined with the values given in Table 1.1, suggest that we would have expected an increase in the muon spectrum of  $< 0.1\%$  for both GLE 71 and 72, which rules their observation with HiSPARC as extremely unlikely and helps explain why we were unable to observe them in the preceding investigation in this chapter. GLE 70 induced a larger increase in the Kiel neutron counts on the order of  $\sim 30\%$ , but comparing this with similar values in Table 1.4 and Table 1.5 suggests we would still only expect an increase in the HiSPARC count rate between  $\sim 0.1 - 2\%$ . In each of these cases it is very unlikely that we would have observed the GLEs using the HiSPARC network.

From these results we must therefore conclude that the HiSPARC network, in its current state, is unable to observe the more abundant standard of GLEs, but it

is likely able to observe the rare, highly energetic events, such as that seen in 1956 leading to GLE 5.

## 1.9 Conclusion

We have presented a feasibility study on using the existing HiSPARC network of muon detectors to monitor space weather events. This was performed through calculating the observing properties of HiSPARC stations, investigating the presence of space weather signatures in the existing data for five HiSPARC stations, both in its raw form and after performing corrections for atmospheric effects, and by performing cosmic ray air shower simulations.

Using simulations of the interactions of CRs with the Earth's magnetosphere in the PLANETOCOSMICS tool, we were able to calculate the rigidity cut-off and AVDs of the HiSPARC stations. We showed that the rigidity cut-off limits the PCRs to particles with energies on the order of and above  $\sim 10^9$  eV. The AVDs were useful in demonstrating that the observable, lower rigidity PCRs are deflected significantly by the Earth's magnetosphere and we may observe solar eruptive events when the station is not pointing in a direction in-line with the Sun.

In the raw HiSPARC data we found that we were unable to clearly detect signatures of the FDs or GLEs that have occurred over the lifetime of the HiSPARC network. It was observed that a major obstructing factor was due to atmospheric effects causing additional variations in the data. Using a linear relationship between the logarithm of the normalised CR counts against both the zero-centred pressure and temperature, the atmospheric effects were removed from the data.

After the removal of the atmospheric effects, when investigating the corrected HiSPARC data we found that we were still unable to observe any GLEs. The same was true for most of the FDs; however, we do speculate that we were able to observe a signature of the FD in December 2014.

A further study was conducted to understand the flux of muons at ground level,

and in particular how the flux varied during GLEs. Using Monte Carlo simulations of particle transport through the atmosphere for incident PCRs, with CORSIKA, we were able to interrogate the number and radial distribution of muons arriving at ground-level per PCR. This highlighted that the flux of muons is very low for PCRs with energies less than, or in the region of, the rigidity cut-off of the HiSPARC stations. This analysis therefore showed that any increase in the CR count from GLEs would likely be very low, due to the diffuse nature of the air showers induced by the low-energy PCRs that primarily make up the GLE-inducing SEP spectra. To observe events with HiSPARC we are excluded to only the most energetic events that are sufficient to produce large muons Air Showers (ASs).

Expanding on this analysis, a comparative study was conducted using the MAIRE tool. This allowed us to directly predict the increase in CR counts based on simulations of incident PCRs, comparing the output muon flux from GCRs and GLEs. A calibration was necessary to ensure that the MAIRE predictions were consistent with the NMDB observations; however, upon applying this calibration, we were able to show that the predicted increase in the muon count rate was significantly lower than the neutron count rate, for each of the six GLEs studied. This led us to conclude that the HiSPARC network is only capable of observing the most energetic GLEs, which occur less frequently than their lower energy equivalents.

We leave the reader with the following points:

1. The rigidity cut-off and AVDs of the HiSPARC stations were calculated using PCR transport simulations. We found the HiSPARC stations generally have a cut-off rigidity in the range,  $R_C \sim 3.0 - 3.5$  GV, setting a limit on the PCRs observable on the order of  $\sim 10^9$  eV. The asymptotic viewing directions for the HiSPARC stations are close to equatorial for low rigidity PCRs, between  $\pm 20^\circ$  in latitude, and tend towards the station's zenith for rigidities greater than 20 GV.
2. Investigations of the raw and atmospheric corrected data showed no signatures

of GLEs in the HiSPARC data. We propose that one FD was observed as a  $\sim 2\%$  decrease in the atmospheric corrected data; however, none of the other events were observed in the HiSPARC data.

3. The CORSIKA air shower simulations showed that the flux of muons at ground level from low-energy CRs ( $\sim 10^9$  eV) is very low, with diffuse air showers. With the current configuration of the HiSPARC network, which strongly relies on the triggering of multiple detectors within a station, the observations are biased to higher energies, hence showing a limitation of the HiSPARC network for space weather observations.
4. The MAIRE simulations showed that for some of the largest GLEs to-date, the predicted increase in the HiSPARC count rate was, on average, no more than  $\sim 1\%$ . Only the most energetic events, with a low occurrence, would induce an increase in the HiSPARC count rate by  $> 5\%$ . This showed that the HiSPARC stations are therefore generally incompatible with monitoring the lower limits of space weather activity, and only suitable as a monitor of the rarer and more extreme events.

This investigation has shown that the feasibility of using the HiSPARC network as a reliable tool for the monitoring of space weather is low; however, we have shown that for some specific cases, we expect to be able to make observations. One of the major issues with the HiSPARC network in its current configurations is the design of the stations. The triggering of multiple detectors biases the stations to observe higher energy PCRs. Since 2016, several HiSPARC stations have been providing the count rates of the individual detectors (the singles rates), which overcomes this biasing problem; however, this data is often inconsistent between stations and also demonstrates a strong diurnal variation that we believe is the manifestation of thermal noise.

The current method of removing the temperature-induced diurnal variation uses

the atmospheric temperature, and not the temperature inside of the rooftop boxes, as it is the only temperature data available. We believe monitoring the temperature in the boxes themselves would provide a more accurate measure of the PMT temperature and hence the thermally induced noise, thus it will show a stronger relationship and provide a more accurate removal of this variation in the data. To overcome these effects, in the next chapter, we investigate the benefits of changing the configuration of a HiSPARC station, to determine whether we can improve the capabilities of the HiSPARC network to monitor space weather.

# A Simulations of Cosmic Ray Air Showers using CORSIKA

There are several user-definable settings within Cosmic Ray Simulations for Kascade (CORSIKA). These settings are explained in-depth in the CORSIKA user’s guide ([Heck & Pierog, 2017](#)). Here, the options selected when building and using CORSIKA are outlined.

For high energy, inelastic hadronic interactions within CORSIKA the QGSJET-II ([Ostapchenko, 2006](#)) model was selected. Interactions of hadrons with energies below 80 GeV are simulated using GHEISHA ([Fesefeldt, 1985](#)), which allowed for the simulation of Primary Cosmic Rays (PCRs) in the regime of Solar Cosmic Rays (SCRs). In addition to these hadronic interactions, electromagnetic interactions within the CORSIKA simulations were described by the EGS4 ([Nelson et al., 1985](#)) model. Furthermore CORSIKA has a minimum muon energy limit that can be simulated of 10 MeV. This limit is sufficient, as the lowest energy muons that are observable with HiSPARC are those with energy of  $\sim 4$  MeV.

Simulation thinning was enabled to reduce the computation time of the simulations and reduce the output file size. The observation level at which point the simulation cease was set at 100 m above sea level (compared to the  $\sim 50$  m typical of the stations; however, this difference is negligible for the air shower development). The pre-defined central European atmosphere in October was used for all simulations, and western-European magnetic field was used as calculated with the *Geomag*

programme ([BGS, 2020](#)):  $B_x = 18.799 \mu\text{T}$  and  $B_z = 44.980 \mu\text{T}$ .

Proton and  $\alpha$ -particle initiated air showers were generated with energies ranging from  $10^9$  to  $10^{20}$  eV, and  $4 \times 10^9$  to  $10^{20}$  eV, respectively. In total  $\sim 230000$  proton-initiated showers were simulated and  $\sim 180000$   $\alpha$ -particle-initiated air showers were simulated. The simulated air-shower-initiating PCRs are listed Table A.1 (proton) and Table A.2 ( $\alpha$ -particles).

Table A.1: Details of the proton-initiated air showers simulated using CORSIKA.

<b>E<sub>PCR</sub> (eV)</b>	<b>N<sub>sims</sub></b>	<b>E<sub>PCR</sub> (eV)</b>	<b>N<sub>sims</sub></b>
1.00E+09	10000	2.98E+12	1000
1.27E+09	10000	3.79E+12	1000
1.62E+09	10000	4.83E+12	1000
2.07E+09	10000	6.16E+12	1000
2.64E+09	10000	7.85E+12	1000
3.36E+09	10000	1.00E+13	1000
4.28E+09	10000	1.78E+13	100
5.46E+09	10000	3.16E+13	100
6.95E+09	10000	5.62E+13	100
8.86E+09	10000	1.00E+14	100
1.00E+10	10000	1.78E+14	50
1.13E+10	10000	3.16E+14	50
1.44E+10	10000	5.62E+14	50
1.83E+10	10000	1.00E+15	10
2.34E+10	10000	1.78E+15	10
2.98E+10	10000	3.16E+15	10
3.79E+10	10000	5.62E+15	10
4.83E+10	10000	1.00E+16	10
6.16E+10	10000	1.78E+16	10
7.85E+10	10000	3.16E+16	10
1.00E+11	10000	5.62E+16	10
1.27E+11	1000	1.00E+17	10
1.62E+11	1000	1.78E+17	10
2.07E+11	1000	3.16E+17	10
2.64E+11	1000	5.62E+17	10
3.36E+11	1000	1.00E+18	10
4.28E+11	1000	1.78E+18	10
5.46E+11	1000	3.16E+18	10
6.95E+11	1000	5.62E+18	10
8.86E+11	1000	1.00E+19	10
1.13E+12	1000	1.78E+19	10
1.44E+12	1000	3.16E+19	10
1.83E+12	1000	5.62E+19	10
2.34E+12	1000	1.00E+20	10

Table A.2: Details of the  $\alpha$ -particle-initiated air showers simulated using CORSIKA.

<b>E<sub>PCR</sub> (eV)</b>	<b>N<sub>sims</sub></b>	<b>E<sub>PCR</sub> (eV)</b>	<b>N<sub>sims</sub></b>
4.00E+09	10000	1.00E+13	1000
4.28E+09	10000	1.78E+13	100
5.46E+09	10000	3.16E+13	100
6.95E+09	10000	5.62E+13	100
8.86E+09	10000	1.00E+14	100
1.00E+10	10000	1.78E+14	50
1.13E+10	10000	3.16E+14	50
1.44E+10	10000	5.62E+14	50
1.83E+10	10000	1.00E+15	10
2.34E+10	10000	1.78E+15	10
2.98E+10	10000	3.16E+15	10
3.79E+10	10000	5.62E+15	10
4.83E+10	10000	1.00E+16	10
6.16E+10	10000	1.78E+16	10
7.85E+10	10000	3.16E+16	10
1.00E+11	10000	5.62E+16	10
1.27E+11	1000	1.00E+17	10
1.62E+11	1000	1.78E+17	10
2.07E+11	1000	3.16E+17	10
2.64E+11	1000	5.62E+17	10
3.36E+11	1000	1.00E+18	10
4.28E+11	1000	1.78E+18	10
5.46E+11	1000	3.16E+18	10
6.95E+11	1000	5.62E+18	10
8.86E+11	1000	1.00E+19	10
1.13E+12	1000	1.78E+19	10
1.44E+12	1000	3.16E+19	10
1.83E+12	1000	5.62E+19	10
2.34E+12	1000	1.00E+20	10
2.98E+12	1000		
3.79E+12	1000		
4.83E+12	1000		
6.16E+12	1000		
7.85E+12	1000		

# Bibliography

- Arunbabu K. P., et al., 2015, *Astronomy and Astrophysics*, 580, A41
- Augusto C., Navia C., de Oliveira M. N., Fauth A., Nepomuceno A., 2016, *Publ Astron Soc Jpn Nihon Tenmon Gakkai*, 68
- BGS 2020, World Magnetic Model Calculator, [http://www.geomag.bgs.ac.uk/data-service/models\\_compass/wmm\\_calc.html](http://www.geomag.bgs.ac.uk/data-service/models_compass/wmm_calc.html)
- Bartels R. T., 2012, Technical report, The HiSPARC Experiment: An Analysis of the MPV and the Number of Events per Unit Time. University College Utrecht
- Belov A. V., 2008, *Proceedings of the International Astronomical Union*, 4, 439
- Belov A. V., Eroshenko E. A., Oleneva V. A., Struminsky A. B., Yanke V. G., 2001, *Advances in Space Research*, 27, 625
- Belov A., Eroshenko E., Mavromichalaki H., Plainaki C., Yanke V., 2005, *Annales Geophysicae*, 23, 2281
- Belov A. V., Eroshenko E. A., Kryakunova O. N., Kurt V. G., Yanke V. G., 2010, *Geomagn. Aeron.*, 50, 21
- Belov A., et al., 2014, *Solar Physics*, 289, 3949
- Berkova M. D., Belov A. V., Eroshenko E. A., Yanke V. G., 2011, *Bull. Russ. Acad. Sci. Phys.*, 75, 820
- Blackmore E. W., Stukel M., Trinczek M., Slayman C., Wen S., Wong R., 2015, *IEEE Transactions on Nuclear Science*, 62, 2792
- Braun I., Engler J., Hrandel J. R., Milke J., 2009, *Advances in Space Research*, 43, 480
- Cecchini S., Sioli M., 2000, arXiv:hep-ex/0002052
- Corti C., Potgieter M. S., Bindi V., Consolandi C., Light C., Palermo M., Popkow A., 2019, *ApJ*, 871, 253
- Cramp J. L., 1996, PhD Thesis, University of Tasmania, Hobart, <https://core.ac.uk/download/pdf/33327719.pdf>
- Danilova O. A., Demina I. M., Ptitsyna N. G., Tyasto M. I., 2019, *Geomagnetism and Aeronomy*, 59, 147

- De Mendonça R. R. S., Raulin J. P., Echer E., Makhmutov V. S., Fernandez G., 2013, *J. Geophys. Res. Space Physics*, 118, 1403
- Desorgher L., 2005, Technical Report PLANETOCOSMICS-SUM, PLANETOCOSMICS Software User Manual, <http://cosray.unibe.ch/~laurent/planetocosmics/>. University of Bern
- Desorgher L., Flckiger E. O., Gurtner M., 2006. p. 2361, <http://adsabs.harvard.edu/abs/2006cosp...36.2361D>
- Dorman L. I., 1972, Kosm. Luchi, no. 13, pp. 5-66
- Dorman L. I., 2004, in Astrophysics and Space Science Library, Cosmic Rays in the Earths Atmosphere and Underground. Springer, Dordrecht, pp 289–330, doi:10.1007/978-1-4020-2113-8\_5, [https://link.springer.com/chapter/10.1007/978-1-4020-2113-8\\_5](https://link.springer.com/chapter/10.1007/978-1-4020-2113-8_5)
- Dorman L. I., 2010, *Phys.-Usp.*, 53, 496
- Dubey A., Kumar S., Dubey S. K., 2016, *Journal of Physics: Conference Series*, 755, 012056
- Dumbović M., Vršnak B., Čalogović J., 2016, *Sol Phys*, 291, 285
- Dyer C. S., Lei F., Clucas S. N., Smart D. F., Shea M. A., 2003, *Advances in Space Research*, 32, 81
- Fesefeldt H., 1985, Technical Report PTHA-85/02, GHEISHA. The Simulation of Hadronic Showers: Physics and Applications. RWTH Aachen
- Fokkema D. B. R. A., 2012, PhD thesis, University of Twente
- Fokkema D. B. R. A., de Laat A. P. L. S., Kooij T., 2012, SAPPHIRE, <https://github.com/HiSPARC/sapphire>
- Forbush S. E., 1937, *Physical Review*, 51, 1108
- Heck D., Pierog T., 2017, Technical Report 7.6400, Extensive Air Shower Simulation with CORSIKA: A Users Guide
- Herbst K., Kopp A., Heber B., 2013, *Annales Geophysicae*, 31, 1637
- Humble J. E. Duldig M. L. Smart D. F. Shea M. A. 2012, *Geophysical Research Letters*, 18, 737
- Kudela K., Storini M., Hofer M. Y., Belov A., 2000, *Space Science Reviews*, 93, 153
- Kuwabara T., et al., 2006a, *Space Weather*, 4, S08001
- Kuwabara T., Bieber J. W., Clem J., Evenson P., Pyle R., 2006b, *Space Weather*, 4, S10001
- Lei F., Clucas S., Dyer C., Truscott P., 2004, *IEEE Transactions on Nuclear Science*, 51, 3442

- Lingri D., Mavromichalaki H., Belov A., Eroshenko E., Yanke V., Abunin A., Abunina M., 2016, arXiv:1612.08900 [astro-ph]
- McCracken K. G., Moraal H., Shea M. A., 2012, *ApJ*, 761, 101
- Mendonça R. R. S. d., et al., 2016, *ApJ*, 830, 88
- Mishev A. L., Usoskin I. G., Raukunen O., Paassilta M., Valtonen E., Kocharov L. G., Vainio R., 2018, *Solar Physics*, 293
- Mishra R. K., Mishra R. A., 2007, *Pramana*, 68, 407
- Mishra R. K., Mishra R. A., 2008, *Rom. Journ. Phys.*, 53, 925
- NMDB 2018, NMDB Event Search Tool (NEST), <http://www.nmdb.eu/nest/>
- Nelson W. R., Hirayama H., Rogers D. W. O., 1985, Technical Report SLAC-265, EGS4 code system, <https://www.osti.gov/biblio/6137659-egs4-code-system>. Stanford Linear Accelerator Center, Menlo Park, CA (USA)
- Ostapchenko S., 2006, *Nuclear Physics B - Proceedings Supplements*, 151, 143
- Owens M. J., Forsyth R. J., 2013, *Living Rev. Sol. Phys.*, 10, 5
- Paschalis P., Mavromichalaki H., Yanke V., Belov A., Eroshenko E., Gerontidou M., Koutroumpi I., 2013, *New Astronomy*, 19, 10
- Pereira E. G., Vasconcellos C. A. Z., Hadjimichel D., 2020, arXiv:2011.06480 [hep-ex, physics:hep-ph]
- Poluianov S., Usoskin I. G., 2017, in Proceedings of Science. Bexco, Busan, Korea, <https://pos.sissa.it/301/#session-3145>
- Rockenbach M., et al., 2014, *Space Sci Rev*, 182, 1
- Savić M., Maletić D., Joković D., Veselinović N., Banjanac R., Udrović V., Dragić A., 2015, *J. Phys.: Conf. Ser.*, 632, 012059
- Schwenn R., 2006, *Living Reviews in Solar Physics*, 3, 2
- Shea M. A., Smart D. F., 1982, *Space Science Reviews*, 32, 251
- Shea M. A., Smart D. F., McCracken K. G., 1965, *J. Geophys. Res.*, 70, 4117
- Strauss R. D., Ogunjobi O., Moraal H., McCracken K. G., Caballero-Lopez R. A., 2017, *Solar Physics*, 292, 51
- Thébault E., et al., 2015, *Earth, Planets and Space*, 67, 79
- Thomas S., Owens M., Lockwood M., Owen C., 2017, *Ann. Geophys.*, 35, 825
- Timashkov D. A., et al., 2008, *Astroparticle Physics*, 30, 117
- Tsyganenko N. A., 1989, *Planetary and Space Science*, 37, 5
- Tsyganenko N. A., 2013, *Annales Geophysicae*, 31, 1745

Usoskin I. G., Braun I., Gladysheva O. G., Hörandel J. R., Jmsn T., Kovaltsov G. A., Starodubtsev S. A., 2008, *J. Geophys. Res.*, 113, A07102

Usoskin I., Ibragimov A., Shea M. A., Smart D., 2016, in Proceedings of The 34th International Cosmic Ray Conference PoS(ICRC2015). Sissa Medialab, The Hague, The Netherlands, p. 054, doi:10.22323/1.236.0054, <https://pos.sissa.it/236/054>

Wawrzynczak A., Alania M. V., 2010, *Advances in Space Research*, 45, 622

Zyla, P. A. (Particle Data Group) et al., 2020, *Progress of Theoretical and Experimental Physics*, 2020

van Dam K., van Eijk B., Fokkema D. B. R. A., van Holten J. W., de Laat A. P. L. S., Schultheiss N. G., Steijger J. J. M., Verkooijen J. C., 2020, *Nuclear Instruments and Methods in Physics Research Section A: Accelerators, Spectrometers, Detectors and Associated Equipment*, 959, 163577